ACCSCIENCE PUBLISHING

Journal of Seismic Exploration

ARTICLE

Random noise suppression in node seismometer signals using improved complete ensemble empirical mode decomposition with adaptive noise and grey relational analysis

Cong Pang[1,2], Tianwen Zhao[3], Guoqing Chen[4,5], Yuxuan Liang[4], Xingxing Li[1], Ya Xiang[1], Sirui Liu[1], and Piyapatr Busababodhin[5]*

[1]Institute of Seismology, China Earthquake Administration, Wuhan, Hubei, China

[2]Wuhan Gravitation and Solid Earth Tides, National Observation and Research Station, Wuhan, Hubei, China

[3]Department of Trade and Logistics, Daegu Catholic University, Gyeongsan, Daegu, Republic of Korea

[4]Mathematical Modeling Research Center, Chengdu Jincheng College, Chengdu, Sichuan, China

[5]Department of Mathematics, Faculty of Science, Mahasarakham University, Kantharawichai, Maha Sarakham, Thailand

Abstract

Node seismometer signals are often contaminated with substantial environmental noise due to the complex conditions encountered in geophysical exploration and seismic monitoring. This necessitates high precision in the pre-processing of ground motion signals, as inadequate processing may compromise subsequent operations, such as P-wave first-arrival time extraction, peak energy calculation, ground motion period determination, and magnitude estimation. To obtain more authentic seismic waveforms, a node seismometer signal denoising model is proposed. This model integrates grey relational analysis (GRA) with improved complete ensemble empirical modal decomposition adaptive noise (ICEEMDAN). This method first decomposes the noisy signal using ICEEMDAN to obtain multiple intrinsic mode functions (IMFs), which are then sequentially arranged and labeled. Subsequently, for each IMF, the correlation coefficient, mutual information, R^2, adjusted R^2, Jensen–Shannon divergence, cosine similarity, root mean squared error, mean absolute error, mean absolute percentage error, and sample entropy were calculated, forming an evaluation matrix for assessing the reliability of all IMFs. Finally, using GRA, the correlation coefficients and degrees of association between each evaluation metric and different IMF components were calculated. The IMF components were ranked based on their association degrees to determine the relative effectiveness of their signal components. Linear reconstruction on the top-ranked IMF components was performed to complete the signal denoising process proposed. Experiments on denoising simulated seismic signals, recorded seismic event signals, and recorded ground motion signals all demonstrate that the GRA–ICEEMDAN model outperforms classical denoising methods. The comprehensive denoising scores for the three experiments were 100, 98.0180, and 93.9056, respectively, with signal-to-noise ratio improvements reaching 24.0049 dB, 20.8926 dB, and 16.3523 dB, respectively. The model effectively distinguishes noise components from effective components, with minimal reconstruction errors

***Corresponding author:**
Piyapatr Busababodhin
(65010263001@msu.ac.th)

Citation: Pang C, Zhao T, Chen G, *et al.* Random noise suppression in node seismometer signals using improved complete ensemble empirical mode decomposition with adaptive noise and grey relational analysis. *J Seismic Explor.* doi: 10.36922/JSE025440098

Received: October 30, 2025

Revised: December 22, 2025

Accepted: December 29, 2025

Published online: March 4, 2026

and signal loss after original signal decomposition, making it suitable for seismic monitoring and geophysical exploration involving small-to-medium sample sizes.

Keywords: Node seismometer; Random noise suppression; Improved complete ensemble empirical modal decomposition adaptive noise; Grey relational analysis; Seismic signal denoising; Ground pulsation signal denoising

1. Introduction

As exploration tasks become increasingly complex and exploration accuracy requirements continue to increase, node seismometers, as a new type of seismic data acquisition equipment, have gradually become an important technical means for high-density seismic acquisition due to their cable-free design, flexible deployment, and adaptability to complex environments.[1-3] Compared with traditional wired seismometers, node seismometers have demonstrated significant advantages in complex surface areas (such as mountain canyons, swamps and lakes, and urban underground spaces), effectively overcoming the deployment limitations of wired systems and improving acquisition efficiency. However, node seismometers still face severe challenges in practical applications. Due to the use of wireless data transmission and the complex working environment, the acquired seismic signals are more susceptible to environmental noise, instrument electronic noise, and random interference, resulting in signal quality degradation.[4-6]

Given the increasing use of velocity-type node seismic instruments in mobile seismic activity monitoring and underground active fault detection, there is a strong practical need to study data pre-processing methods, such as denoising. By reducing the random environmental noise content in the original signal, the quality of seismic data can be further improved, thereby enhancing the accuracy of extracting parameters, such as the first arrival time of the first wave.

The core of seismic signal denoising algorithms lies in completely suppressing noise while maintaining the waveform characteristics and dynamic characteristics of the effective signal to avoid distortion. Seismic signal denoising methods have evolved from traditional Fourier analysis to modern time–frequency analysis. Early methods were mainly based on the frequency domain characteristics of the signal, such as the Fourier transform and bandpass filtering. These methods assumed that the signal and noise were separable in the frequency domain; exhibiting good results for stationary signal processing.[7-11] However, actual seismic signals have the characteristics of non-stationary and non-minimum phase. Traditional frequency domain methods often damage the effective signal while denoising, especially the phase information of waveform mutations.

Wavelet transform, as an important tool for time–frequency analysis, realizes multi-scale analysis of non-stationary signals through adjustable time–frequency windows and has been widely used in the field of seismic denoising.[12] The threshold denoising method based on wavelet transform achieves signal–noise separation by setting an appropriate threshold according to the different performances of signal and noise in the wavelet domain, suppressing high-frequency noise while enhancing the ability to retain low-frequency effective signals. However, the effect of the wavelet transform depends largely on the selection of the wavelet basis function and decomposition scale, and its adaptability to transient components in non-stationary signals is limited.

To overcome the shortcomings of the wavelet transform, the empirical mode decomposition (EMD) method was introduced into the field of signal processing.[13] EMD performs adaptive decomposition based on the local characteristic time scale of the signal, decomposing complex signals into a series of intrinsic mode functions (IMFs), which are very suitable for processing non-stationary and non-linear signals. However, traditional EMD faces challenges, such as modal aliasing and endpoint effects, which affect the stability and reliability of the decomposition. To address the shortcomings of EMD, researchers have proposed a series of improved algorithms, such as ensemble EMD (EEMD), complete EEMD (CEEMD), and CEEMD with adaptive noise (CEEMDAN). These algorithms reduce modal mixing and reconstruction errors by introducing noise-assisted analysis.[14-16] Furthermore, improved CEEMDAN (ICEEMDAN) optimizes the noise addition method based on CEEMD. Instead of adding random white noise to the original signal, it performs EMD by introducing a pair of white noises with opposite properties. This can suppress the reconstruction error caused by the introduction of white noise to a certain extent and control the amount of residual noise, resulting in a final decomposition that is more accurate.[17-20]

Denoising methods based on signal decomposition can subdivide the original noisy signal into IMFs with high

noise content, low noise content, and near-noise content. However, after decomposition, common problems exist, such as unclear discrimination of the noise content of IMFs, monotonous and easily discarded IMF waveforms containing the main amplitude energy, and difficulty in selecting the reconstruction targets. An appropriate evaluation index system has not been established to measure the quality or noise content of these IMFs. Hence, an effective evaluation method is urgently needed to accurately identify the effective IMF components that can participate in the final reconstruction and provide a reasonable basis for IMF screening. On the other hand, grey relational analysis (GRA), a mathematical method for measuring the degree of correlation between factors, has been introduced into the field of signal processing in recent years, providing a new criterion for distinguishing signal from noise.[21-23] GRA can adaptively identify the dominant noise component by calculating the geometric similarity between sequences and has demonstrated good performance in image denoising. However, research combining GRA with ICEEMDAN for node seismometer signal processing is still scarce. This technical integration is expected to achieve new breakthroughs in noise suppression and signal fidelity.

To fully utilize the advantages of ICEEMDAN in adaptive decomposition of non-stationary signals and combine the sensitivity of GRA in distinguishing between signals and noise, this study proposes a nodal seismograph signal denoising model based on GRA optimizing CEEMD to solve the problem of random noise interference in nodal seismograph-acquired signals. The model comprehensively considers the correlation coefficient (COEF),[24] mutual information (MI),[25] sample entropy (SE),[26] mean absolute error (MAE),[27] mean absolute percentage error (MAPE),[28] coefficient of determination (also known as R^2),[29] cosine similarity (CS),[30] root mean square error (RMSE),[31] Jensen–Shannon divergence JSD,[32] and adjusted R^2 (Adj-R^2).[33] GRA is then used to pe=rform multi-dimensional compression of the IMF characteristic indicator matrix, thereby constructing a comprehensive evaluation function of the quality of IMF components. Based on the ranking of this function, the original noisy signal is linearly reconstructed. Finally, simulation signal experiments and node seismometer measured signal denoising experiments are designed, and the proposed GRA–ICEEMDAN model is compared with classical denoising models, such as Kalman filtering, low-pass finite impulse response (FIR) filtering, and Savitzky–Golay, to evaluate overall denoising performance.

The main research contents and innovations of this study include:

(i) Application and optimization of the ICEEMDAN signal decomposition method: Using ICEEMDAN to decompose the node seismometer signal into a series of IMF components, optimize the decomposition parameters according to the characteristics of the seismic signal, improve the modal aliasing problem of the traditional EMD algorithm, and lay the foundation for subsequent noise separation.

(ii) Introduction of GRA criteria: GRA is innovatively applied to the classification and discrimination of IMF components. By calculating the grey correlation between each IMF and the noisy original signal, the noise-dominated IMF and the signal-dominated IMF are adaptively distinguished; overcoming the limitations of traditional methods based on COEFs or fixed thresholds.

(iii) Construction of hybrid denoising model: Combining ICEEMDAN with GRA establishes a complete denoising process, including signal adaptive decomposition, IMF component grey correlation calculation, noise component identification and screening, signal reconstruction, and other steps, that effectively suppresses random noise and preserves effective signals.

(iv) Algorithm verification and performance evaluation: Through simulation experiments, ground pulsation signal denoising experiments and earthquake event signal denoising experiments, the effectiveness of the proposed method is systematically verified, and compared with traditional and modern methods, such as Kalman filtering, low-pass FIR filtering, Savitzky–Golay filtering, and others, to evaluate its performance in terms of signal-to-noise ratio (SNR) improvement, RMSE reduction, and waveform fidelity.

(v) Design of comprehensive noise reduction evaluation metrics: To accurately assess the noise reduction capability and fidelity of various noise reduction models, five widely recognized and complementary quantitative evaluation metrics were selected from multiple perspectives, including signal fidelity, noise suppression intensity, and frequency domain feature preservation. These metrics were integrated to design a single comprehensive evaluation metric. The sub-metrics include: SNR improvement, noise suppression rate, correlation, frequency similarity, and energy retention rate. The overall score metric is defined as the sum of the normalized weighted values of the five indicators (with the first indicator in simulation experiments replaced by traditional SNR), where each indicator carries equal weight.

The structure of this study is arranged as follows: Section 1 is the introduction, which introduces the research

background and significance; Section 2 explores the GRA–ICEEMDAN signal denoising model, which elaborates on the denoising model principle and implementation steps of GRA combined with ICEEMDAN; Section 3 systematically analyzes the random noise suppression experiment and analysis of simulated noisy signals; Section 4 provides a report on denoising experiments and analysis of node seismometer recorded signals through two sets of event data with different environmental stimuli, and a comparative analysis of similar filtering models; and lastly, Section 5 summarizes the research results and proposes future research directions.

2. The GRA–improved complete ensemble EMD with adaptive noise signal denoising model

2.1. Analysis of the principles of GRA

GRA is a comprehensive evaluation method for small-sample problems based on the grey system theory and the similarity and difference of indicators to obtain a degree of correlation. It generally goes through several main steps, including data standardization, COEF calculation, correlation degree calculation, and ranking correlation degree. It has many advantages, such as small sample adaptability, no need for strict distribution assumptions, strong noise resistance, and low computational complexity. The general steps for performing correlation analysis between evaluation objects and indicators using GRA are as follows:

(i) Set the number of evaluation objects to m and the number of evaluation indicators to n. Standardize the original data and set the reference sequence and comparison sequence as $x_0 = \{x_0(k)\ k = 1,2,\ldots,n\}, x_i = \{x_i(k) \mid k = 1,2,\ldots,n; i = 1,2,\ldots,m\}$, respectively.

(ii) Determine the corresponding weights of each evaluation indicator and construct a one-dimensional weight vector $w = [w_1, w_2, \ldots, w_n]$, where $w_k (k = 1,2,\ldots,n)$ represents the weight value of the k-th evaluation indicator.

(iii) Set the resolution coefficient $\rho \in [0,1]$. The grey COEF $\xi_i(k)$ between the comparison sequence x_0 and the reference sequence x_i on the k-th evaluation indicator is defined as **Equation 1:**

$$\xi_i(k) = \frac{\min\limits_s \min\limits_t \left|x_0(t) - x_i(t)\right| + \rho \max\limits_s \max\limits_t \left|x_0(t) - x_i(t)\right|}{\left|x_0(k) - x_i(k)\right| + \rho \max\limits_s \max\limits_t \left|x_0(t) - x_i(t)\right|} \quad (1)$$

where, $\min\limits_s \min\limits_t \left|x_0(t) - x_i(t)\right|$ is the minimum difference between the two levels; $\max\limits_s \max\limits_t \left|x_0(t) - x_s(t)\right|$ is the maximum difference between the two levels.

(iv) According to the index weight vector w and $m \times n$ grey COEFs $\xi_i(k)$, the grey weighted correlation degree of the i-th evaluation object is calculated as in **Equation 2:**

$$r_i = \sum_{k=1}^{n} w_i \xi_i(k) \quad (2)$$

(v) Finally, the gray weighted correlation degree obtained in step (iv) is used to score and rank the m evaluation objects. The higher the correlation degree, the higher the credibility of the evaluation object.

2.2. The improved complete ensemble EMD with an adaptive noise signal denoising method

The ICEEMDAN method is a multi-step improvement on the standard EMD technique. Having undergone various stages of development and improvement, including EMD, EEMD, and CEEMDAN, ICEEMDAN introduces a local mean operator to replace direct modal decomposition and optimizes noise injection strategies based on the decomposition of non-stationary and non-linear signals. This overcomes common signal decomposition issues, such as modal aliasing, residual noise, and pseudo-modal components. EMD suffers from modal aliasing. EEMD introduces white noise to balance the original noise, but still leaves residual reconstruction errors and pseudo-components. CEEMDAN reduces reconstruction errors, but the early IMFs still contain residual noise, and signal information is delayed. The main steps for signal decomposition are:

(i) The original signal x is decomposed to construct a noisy synthetic signal (**Equation 3**):

$$x^{(i)} = x + \beta_0 E_1(w^{(i)}) \quad (3)$$

where, β_0 is the signal-to-noise ratio at the first decomposition; $w^{(i)}$ is the i-th Gaussian white noise added; and $E_1(\cdot)$ is the first IMF component obtained by EMD decomposition.

(ii) Repeat the previous step N times to obtain N $x^{(i)}$ and calculate the average of all local mean function values, which is the first residual component, as shown in **Equation 4:**

$$r_1 = \frac{1}{N} \sum_{i=1}^{N} M(x^{(i)}) \quad (4)$$

In the above formula, $M(\cdot)$ is the local mean function.

(iii) The first mode is obtained by subtracting the first residual component from the original signal, as shown in **Equation 5:**

$$d_1 = x - r_1 \quad (5)$$

(iv) Based on the local mean function value calculated after the k-th decomposition, the k-th residual component is obtained, and the residual result of this decomposition is subtracted from the previous residual component to obtain the k-th mode d_m, as shown in **Equations 6** and **7**

$$d_m = r_{k-1} - r_k \tag{6}$$

$$r_k = \frac{1}{N}\sum_{i=1}^{N} M(r_{k-1} + \beta_{k-1} E_k(\omega^{(i)}) \tag{7}$$

(v) Continue executing step (iv) until the decomposition stopping condition is met.

As a data-driven adaptive decomposition method, the number of IMFs generated by ICEEMDAN is not fixed but depends on the time–frequency complexity of the input signal itself and the algorithm's stopping criteria (such as whether the algorithmic residual meets the condition of a monotonic function). Specifically, the richer the oscillatory modes within a signal, the greater the number of IMFs typically decomposed; conversely, fewer IMFs are generated. This adaptability is precisely where it surpasses fixed-basis transforms, such as the wavelet transform, enabling it to more flexibly match the non-stationary characteristics of seismic signals.

2.3. Signal decomposition evaluation metrics and noise reduction effect evaluation metrics

To measure the differences or similarities between each IMF obtained from the ICEEMDAN decomposition and the original signal, and identify the effective and noise components in the IMF component set, thereby achieving high-quality denoising of the original noisy signal, we selected 10 parameters: COEF, MI, SE, MAE, MAPE, R^2, CS, RMSE, JSD, and Adj-R^2. These parameters were used to evaluate the overall performance of all IMFs from multiple perspectives, including waveform similarity, amplitude error, and signal disorder.

The value of JS is between 0 and 1. The value 0 indicates identical distributions, and 1 indicates opposite distributions. JS divergence measures the similarity between two probability distributions. CS is a value between −1 and 1, where 1 indicates identical directions (two vectors are completely similar), and 0 indicates no similarity (two vectors are perpendicular and have completely different directions).

Sample entropy is a characteristic parameter describing the degree of non-stationarity of a signal. If the signal has no obvious distribution pattern, experiences severe local oscillations, or has a lot of noise, the sample entropy value is large, and vice versa. The calculation of N-dimensional signal sample entropy generally involves phase space reconstruction, calculation of reconstructed vector distance, calculation of matching degree, and its mean $B^m(r)$ under the similarity tolerance threshold r, increasing the dimension m to m+1, and repeating the above process to obtain the sample entropy value.

In linear regression, Adj-R^2 is used to correct the spurious improvement in model fit caused by an increase in the number of independent variables. The calculation formulas for all evaluation indicators are as follows in **Equations 8-17**:

$$COEF = \frac{\sum_{i=1}^{n} s(i)y(i)}{\sqrt{\sum_{i=1}^{n} y^2(i)\sum_{i=1}^{n} s^2(i)}} \tag{8}$$

$$MAE = \frac{1}{n}\sum_{i=1}^{n}\left|s(i) - y(i)\right| \tag{9}$$

$$MAPE = \frac{1}{n}\sum_{i=1}^{n}\left|\frac{s(i) - y(i)}{s(i)}\right| \tag{10}$$

$$CS = \frac{\sum_{n=1}^{N}\left(y(i)\cdot s(i)\right)}{\sqrt{\sum_{n=1}^{N} y^2(i)}\cdot\sqrt{\sum_{n=1}^{N} s^2(i)}} \tag{11}$$

$$RMSE = \sqrt{\frac{1}{n}\sum_{i=1}^{n}\left(s(i) - y(i)\right)^2} \tag{12}$$

$$R^2 = 1 - \frac{\sum_{i=1}^{n}\left(s(i) - y(i)\right)^2}{\sum_{i=1}^{n}\left(s(i) - \bar{s}\right)^2} \tag{13}$$

$$JSD = \frac{1}{2}\sum_{i}\left(s(i)\times log\left(2\cdot s(i)/(s(i)+y(i))\right)\right) + \frac{1}{2}\sum_{i}\left(y(i)\times log\left(2\cdot y(i)/(s(i)+y(i))\right)\right) \tag{14}$$

$$MI(Y;S) = \sum_{y\in Y}\sum_{s\in S} p(y,s) log\left(\frac{p(y,s)}{p(y)\cdot(s)}\right) \tag{15}$$

$$SampEn(m,r,N) = -ln\frac{B^{m+1}(r)}{B^m(r)} \tag{16}$$

$$Adj - R^2 = 1 - \frac{\left(1-R^2\right)\left(n-1\right)}{n-p-1} \tag{17}$$

In the above equations: $y(n)$ is the IMF component obtained by ICEEMDAN; $s(n)$ is the original signal; $\bar{s}(n)$ is the mean of the original signal, n is the signal length, p is

the number of independent variables; $p(s,y)$ is the joint probability distribution of discrete variables S and Y; and $p(y)$ and $p(s)$ are the marginal probability distributions of discrete variables S and Y, respectively.

To accurately evaluate the noise reduction capability and fidelity of various denoising models, five widely recognized and complementary quantitative evaluation metrics were selected from multiple perspectives, including signal fidelity, noise suppression intensity, and frequency domain feature preservation. An overall score was designed based on these metrics:

In practical applications lacking pure reference signals, SNR improvement serves as the most direct measure of noise suppression effectiveness. Assuming the signal's useful components are primarily distributed in the low-frequency range, while the high-frequency portion consists mainly of noise, the noise component is estimated separately in both the noisy signal and the denoised signal. The SNR is then calculated for each and compared. The difference between these two SNR values represents the final SNR improvement value, measured in dB. The noise estimation algorithm employs a high-pass filter to isolate high-frequency noise while utilizing a low-pass filter to estimate the signal components.

Assuming the useful signal components are concentrated in the mid-to-low frequency range, the noise suppression rate metric quantifies the degree of noise suppression by comparing the energy changes in the high-frequency portion of the signal before and after denoising. It is defined as the difference between the high-frequency energy ratio of the denoised signal and that of the original signal. This indicator directly quantifies the proportion of noise components removed.

Correlation calculates the Pearson COEF between the denoised signal and either a true clean signal (in simulations) or a noise reference signal (in real data). A high COEF (close to 1) indicates the denoising process effectively preserves the original signal's structure and waveform characteristics, avoiding excessive distortion.

Frequency similarity is defined as the COEF between the spectral value sequences of the pre- and post-denoising signals after the Fourier transform. This objectively evaluates the method's ability to preserve useful signal components in the frequency domain and suppress noise bands.

The denoising process should ensure useful signal energy is not excessively attenuated. Energy retention is defined as the ratio of the energy of the denoised signal (sum of squares at each point) to the energy of the original noisy signal, balancing noise suppression and signal preservation.

Overall score serves as a comprehensive evaluation metric for denoising effectiveness; it is defined as the sum of the normalized weighted values of the above five metrics (with the first metric in simulation experiments replaced by traditional SNR), where each metric carries equal weight.

2.4. Signal denoising process based on the GRA–improved complete ensemble EMD with adaptive noise signal denoising model

The signal processing flow of the GRA–ICEEMDAN denoising model (Figure 1) consists of the following steps:

(i) First, the nodal seismograph signal is decomposed using ICEEMDAN to obtain several IMF components. It is necessary to further distinguish between effective and noisy components before performing IMF reconstruction.

(ii) The COEF, MI, R^2, Adj-R^2, JSD, CS, RMSE, MAE, MAPE, and sample entropy for each of the above IMF components are calculated to construct a 10-dimensional IMF evaluation index matrix.

(iii) GRA is performed on the IMF evaluation index matrix, followed by a sequential standardization, calculation of the minimum/maximum difference between two levels, calculation of grey relational coefficients, index weight estimation, and IMF correlation analysis to obtain the final ranking of all IMF components.

(iv) Finally, the top half of the ranked IMF components is linearly constructed to obtain the denoised nodal seismograph data.

To test the feasibility and denoising effect of the above GRA–ICEEMDAN process, it is necessary to combine some simulation experiments for evaluation. The specific details will be discussed in the experimental analysis section of Sections 3 and 4.

3. Experiment and analysis of random noise suppression for simulated noisy signals

To test the theoretical denoising performance of the GRA–ICEEMDAN model, a simulated noisy signal denoising experiment was introduced. Ten metrics—COEF, sample entropy, MI, R^2, CS, JSD, RMSE, MAE, Adj-R^2, and MAPE—were used to evaluate the quality of several IMF components obtained from the ICEEMDAN decomposition. Then, the denoising model's effectiveness was evaluated using three metrics: COEF, SNR, and MSE. Finally, the denoising performance was compared with several classic models.

The simulation platform used was MATLAB 2024b, with a signal length of 10 s and a sampling rate of 500 Hz. The simulated seismic signal consists of three waveforms (fundamental wave, P-wave, S-wave). The fundamental

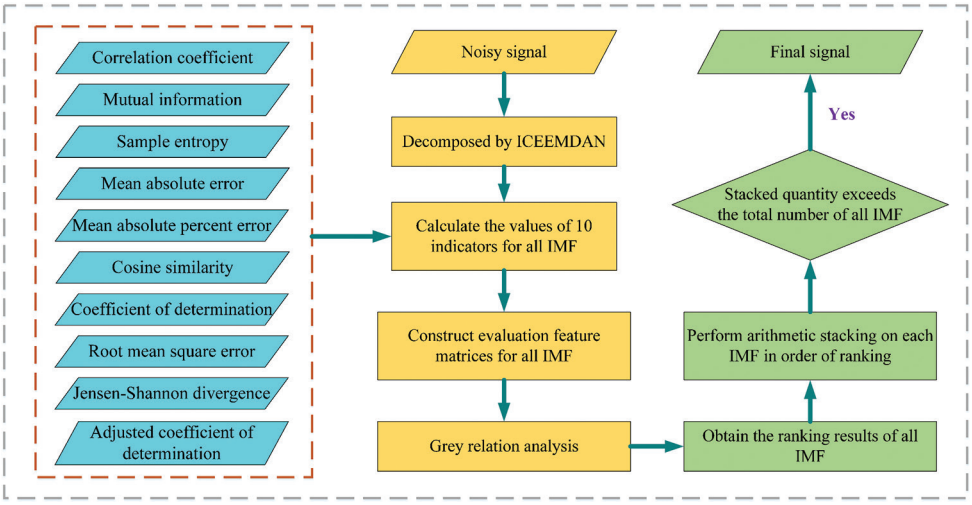

Figure 1. Denoising process of the grey relational analysis–improved complete ensemble empirical mode decomposition with adaptive noise signal denoising model
Abbreviation: IMF: Intrinsic mode function.

wave simulates background microseismic components (low-frequency continuous signal). It generates the base waveform by superimposing multiple low-frequency sine waves across the entire time domain, with the generation function defined as **Equation 18**:

$$y(t) = 1 + \sum_{i=1}^{3} \left(\alpha_i \times \sin\left(2\pi \cdot f_i^{back} \cdot t \right) \right) \tag{18}$$

where α_i = 0.3 or 0.7 or 1.2, and, $f_i^{back} = 0.02 \ or \ 0.06 \ or \ 0.01$.

The P-wave is designed to start at 1 s and last for 1.8 s. It is formed by the Hadamard product of a power function and a sine function, simulating a high-frequency waveform with short duration and relatively small amplitude, that is, $y_p(t_p) = 0.6 \times e^{\alpha_p t_p} \cdot \sin\left(2\pi \cdot f_p \cdot t_p \right)$. The S-wave was designed to start at 2.5 s and last for 4.8 s, composed of the Hadamard product of a power function and a sine function, simulating a low-frequency waveform with larger amplitude and longer duration, that is, $y_s(t_s) = 2 \times (e^{\alpha_s t_s} \cdot (1 - e^{\alpha_s t_s})) \cdot \sin\left(2\pi \cdot f_s \cdot t_s \right)$. By adding 20 SNR/dB of Gaussian white noise to the simulated seismic signal using MATLAB's built-in "awgn" function, the noise-containing signal required for the experiment was generated.

The ICEEMDAN decomposition parameters were set as follows: Noise intensity 0.2, number of integrations 3, and maximum iterations 3,600. The similarity tolerance threshold for sample entropy was defined as 0.15 times the signal standard deviation. The resulting clean signal, noisy signal, and corresponding ICEEMDAN decomposition plots are shown in the subplots of Figure 2.

Table 1 presents the eigenvalues of each IMF component after decomposing the original simulated noisy signal using ICEEMDAN, encompassing 10 distinct metric values. IMF_1 to IMF_2, obtained from decomposing the noisy signal, exhibited high-frequency, low-amplitude random oscillations. Their sample entropy values exceeded 1.5, and their COEFs with the original signal were all below 0.1, with the various error function values (RMSE, MAE, etc.) being relatively large. These characteristics indicate significant amplitude differences between these IMFs and the original signal, suggesting that they represent system noise components that should be removed. IMF_3–IMF_4 exhibited smoother waveforms (sample entropies below 0.06) with pronounced low-frequency characteristics. Their amplitude magnitudes and curve shapes (COEFs exceeding 0.5) aligned more closely with the original signal, qualifying them as valid components extracted from the noisy original signal. The amplitudes of other IMFs were all below 0.1, showing a significant gap compared to the peak value of the original signal (1.9). Whether they need to be retained requires correlation analysis using GRA.

The IMF quality evaluation indicator matrix was derived from Table 1. After undergoing necessary processing steps—including standardization, two-stage least squares/maximum differences calculation, grey relational coefficient computation, subjective assignment of indicator weights, and IMF correlation analysis—the final quality ranking results for IMF components were obtained. The specific calculation results are shown in Tables 2 and 3 and Figure 3. Table 2 presents the comparative sequences and reference sequence values for each IMF in the simulated noisy signal, while Table 3 displays the GRA COEFs and

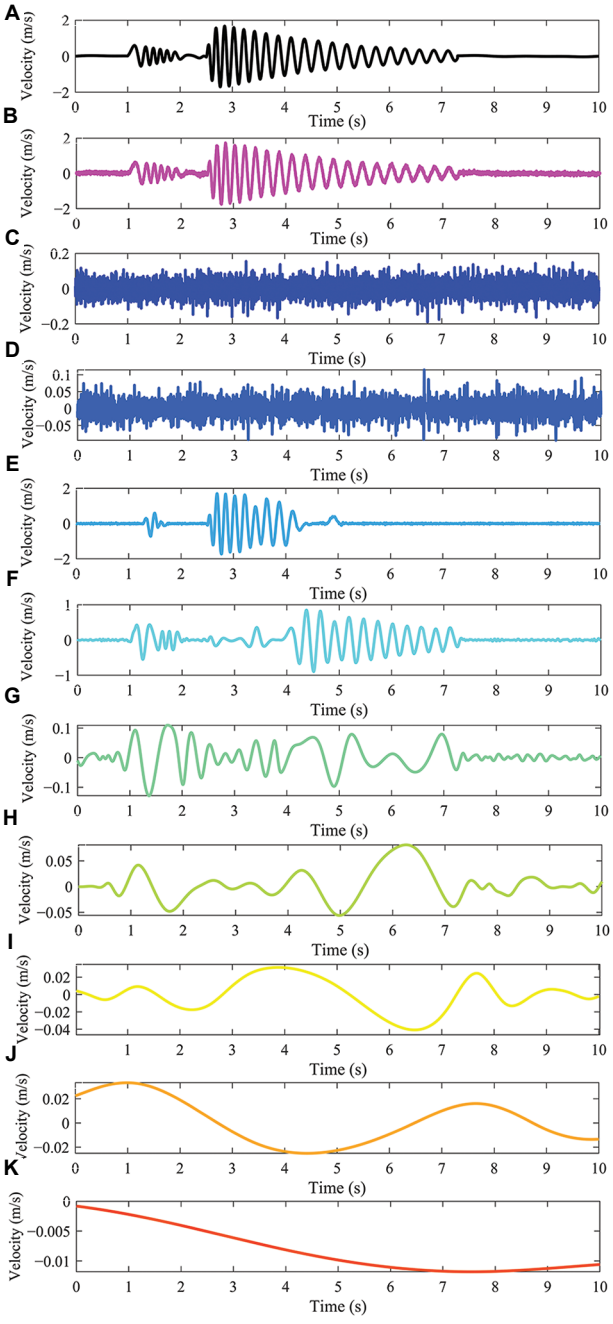

Figure 2. Simulated original signal and improved complete ensemble empirical mode decomposition with adaptive noise signal denoising decomposition results. (A) Original clean signal. (B) Original noisy signal. (C) IMF_1. (D) IMF_2. (E) IMF_3. (F) IMF_4. (G) IMF_5. (H) IMF_6. (I) IMF_7. (J) IMF_8. (K) IMF_9.
Abbreviation: IMF: Intrinsic mode function.

correlation values for each IMF in the simulated noisy signal.

The comparison and reference sequences in Table 2 can be used to construct the GRA COEFs between 10 evaluation indicators and each IMF (Table 3). Based on the balanced indicator weight vector {0.1,0.1,0.1,0.1,0.1,0.1,0.1,0.1,0.1,0.1} and the GRA COEFs, the grey weighted correlation degree of each IMF was obtained using arithmetic average (Table 3).

IMF_3, IMF_8, and IMF_9 achieved the best performance (COEF value of 1) in seven, one, and two out of 10 evaluation metrics, respectively, indicating that IMF_8 exhibited the most significant correlation with the original signal. Specifically, IMF_3 attained the highest scores in seven metrics, including COEF, Adj-R^2, MAE, CS, RMSE, R^2, and JSD correlation; IMF_8 only outperformed in the MI metric, while IMF_9 stood out in metrics, such as sample entropy and MAPE. In the comprehensive ranking (IMF_3 > IMF_4 > IMF_9 > IMF_7 > IMF_8 > IMF_5 > IMF_6 > IMF_2 > IMF_1), although IMF_4 did not achieve the optimal GRA COEF in any single metric, its COEFs exceeded 0.5 across six metrics, indicating it also captured key signal components. Therefore, the top five IMF models (IMF_3, IMF_4, IMF_7, IMF_8, IMF_9) were selected for linear reconstruction.

To compare the GRA–ICEEMDAN model's superiority among similar signal denoising principles, nine reference models—wavelet threshold denoising, median filter, Wiener filter, Savitzky–Golay filter, elliptic filter, Butterworth filter, Kalman filter, Chebyshev filter, and moving average filter—were used. The evaluation framework incorporated quantitative metrics across multiple dimensions, including SNR, noise suppression ratio, correlation, frequency similarity, energy retention, and overall score. The denoising results for each model are presented in Figure 3.

Compared to the significant phase delays and severe waveform distortion observed in other models, the wavelet, median filter, Wiener filter, and GRA–ICEEMDAN models demonstrated positive effects in seismic signal denoising, achieving a degree of smoothing and high time-frequency fidelity (Figure 3A-C). The 0.5-s local magnification (Figure 3C) reveals substantial differences in local characteristics among the 10 denoising models, with varying degrees of divergence in amplitude magnitude, phase delay, frequency, and peak energy. Among these, the wavelet and GRA–ICEEMDAN models exhibited smoother and more stable waveform processing at peaks or troughs, while the Chebyshev denoising results completely lost all original signal characteristics. Issues with other models were primarily centered on phase delays (0.025–0.05 s) and amplitude reductions.

This scale disparity was also pronounced in the spectral plots, with spectral curve differences among models primarily concentrated in the low-to-mid frequency

Table 1. Characteristic index values of each IMF after ICEEMDAN decomposition of the simulated noisy signal

IMF components	Correlation coefficient	Sample entropy	CS	R^2	JSD	RMSE	MAE	MAPE	Adj-R^2	MI
IMF_1	0.0719	2.2866	0.0718	0.0047	0.4131	0.4682	0.2924	2.8243	0.0049	0.8379
IMF_2	0.0437	1.5415	0.0439	0.0017	0.4242	0.4689	0.2961	2.0493	0.0017	0.8355
IMF_3	0.8479	0.0198	0.8479	0.7189	0.1692	0.2488	0.1665	6.5080	0.7189	0.6970
IMF_4	0.5247	0.0544	0.5248	0.2750	0.2080	0.3996	0.1921	8.1701	0.2752	0.7920
IMF_5	0.0210	0.0762	0.0216	−0.0039	0.3815	0.4702	0.2958	2.7874	0.0002	0.8423
IMF_6	0.0084	0.0266	0.0094	−0.0027	0.4372	0.4699	0.2972	2.8712	−0.0001	0.8473
IMF_7	0.0190	0.0142	0.0186	−0.0001	0.3512	0.4693	0.2968	2.1045	0.0001	0.8655
IMF_8	0.0282	0.0049	0.0288	0.0006	0.5020	0.4691	0.2964	2.4613	0.0005	0.8714
IMF_9	0.0283	0.0007	0.0025	−0.0003	0.3233	0.4694	0.2974	1.7733	0.0006	0.8653

Abbreviations: Adj-R^2: Adjusted coefficient of determination; CS: Cosine similarity; ICEEMDAN: Improved complete ensemble empirical mode decomposition with adaptive noise signal denoising; IMF: Intrinsic mode function; JSD: Jensen–Shannon divergence; MAE: Mean absolute error; MAPE: Mean absolute percentage error; MI: Mutual information; R^2: Coefficient of determination; RMSE: Root mean square error.

Table 2. Comparison series and reference series values of each IMF of the simulated noisy signal

Serial no.	Evaluation indicators	IMF_1	IMF_2	IMF_3	IMF_4	IMF_5	IMF_6	IMF_7	IMF_8	IMF_9	Optimal IMF
1	Correlation coefficient	0.0756	0.0419	1	0.6149	0.0149	0	0.0125	0.0235	0.0237	1
2	Sample entropy	0	0.3259	0.9916	0.9765	0.9670	0.9886	0.9940	0.9981	1	1
3	CS	0.0819	0.0489	1	0.6177	0.0226	0.0083	0.0190	0.0311	0	1
4	R^2	0.0121	0.0079	1	0.3859	0	0.0016	0.0052	0.0063	0.0049	1
5	JSD	0.2671	0.2338	1	0.8833	0.3620	0.1945	0.4531	0	0.5368	1
6	RMSE	0.0092	0.006088	1	0.3190	0	0.0012	0.0039	0.0048	0.0038	1
7	MAE	0.0378	0.0097	1	0.8041	0.0118	0.0010	0.0040	0.0075	0	1
8	MAPE	0.8356	0.9568	0.2598	0	0.8414	0.8283	0.9482	0.8924	1	1
9	Adj-R^2	0.0071	0.0025	1	0.3828	0.0005	0	0.0004	0.0010	0.0010	1
10	MI	0.8077	0.7938	0	0.5446	0.8330	0.8618	0.9663	1	0.9651	1

Abbreviations: Adj-R^2: Adjusted coefficient of determination; CS: Cosine similarity; IMF: Intrinsic mode function; JSD: Jensen–Shannon divergence; MAE: Mean absolute error; MAPE: Mean absolute percentage error; MI: Mutual information; R^2: Coefficient of determination; RMSE: Root mean square error.

Table 3. Grey relation analysis, correlation coefficients, and correlation values of each IMF in the simulated noisy signal

Serial number	Evaluation indicators	The IMF evaluated								
		IMF_1	IMF_2	IMF_3	IMF_4	IMF_5	IMF_6	IMF_7	IMF_8	IMF_9
1	Correlation coefficient	0.3510	0.3429	1	0.5649	0.3366	0.3333	0.3361	0.3386	0.3386
2	Sample entropy	0.3333	0.4258	0.9836	0.9551	0.9380	0.9778	0.9883	0.9963	1
3	CS	0.3526	0.3445	1	0.5667	0.3384	0.3351	0.3376	0.3404	0.3333
4	R^2	0.3360	0.3351	1	0.4488	0.3333	0.3336	0.3344	0.3347	0.3344
5	JSD	0.4055	0.3948	1	0.8108	0.4393	0.3829	0.4776	0.3333	0.5191
6	RMSE	0.3354	0.3346	1	0.4233	0.3333	0.3336	0.3342	0.3344	0.3341
7	MAE	0.3419	0.3355	1	0.7185	0.3359	0.3335	0.3342	0.3350	0.3333
8	MAPE	0.7526	0.9205	0.4031	0.3333	0.7592	0.7444	0.9061	0.8229	1
9	Adj-R^2	0.3349	0.3339	1	0.4475	0.3334	0.3333	0.3334	0.3335	0.3335
10	MI	0.7223	0.7080	0.3333	0.5233	0.7496	0.7835	0.9370	1	0.9348
11	Correlation	0.4265	0.4476	0.8720	0.5792	0.4897	0.4891	0.5319	0.5169	0.5461

Abbreviations: Adj-R^2: Adjusted coefficient of determination; CS: Cosine similarity; IMF: Intrinsic mode function; JSD: Jensen–Shannon divergence; MAE: Mean absolute error; MAPE: Mean absolute percentage error; MI: Mutual information; R^2: Coefficient of determination; RMSE: Root mean square error.

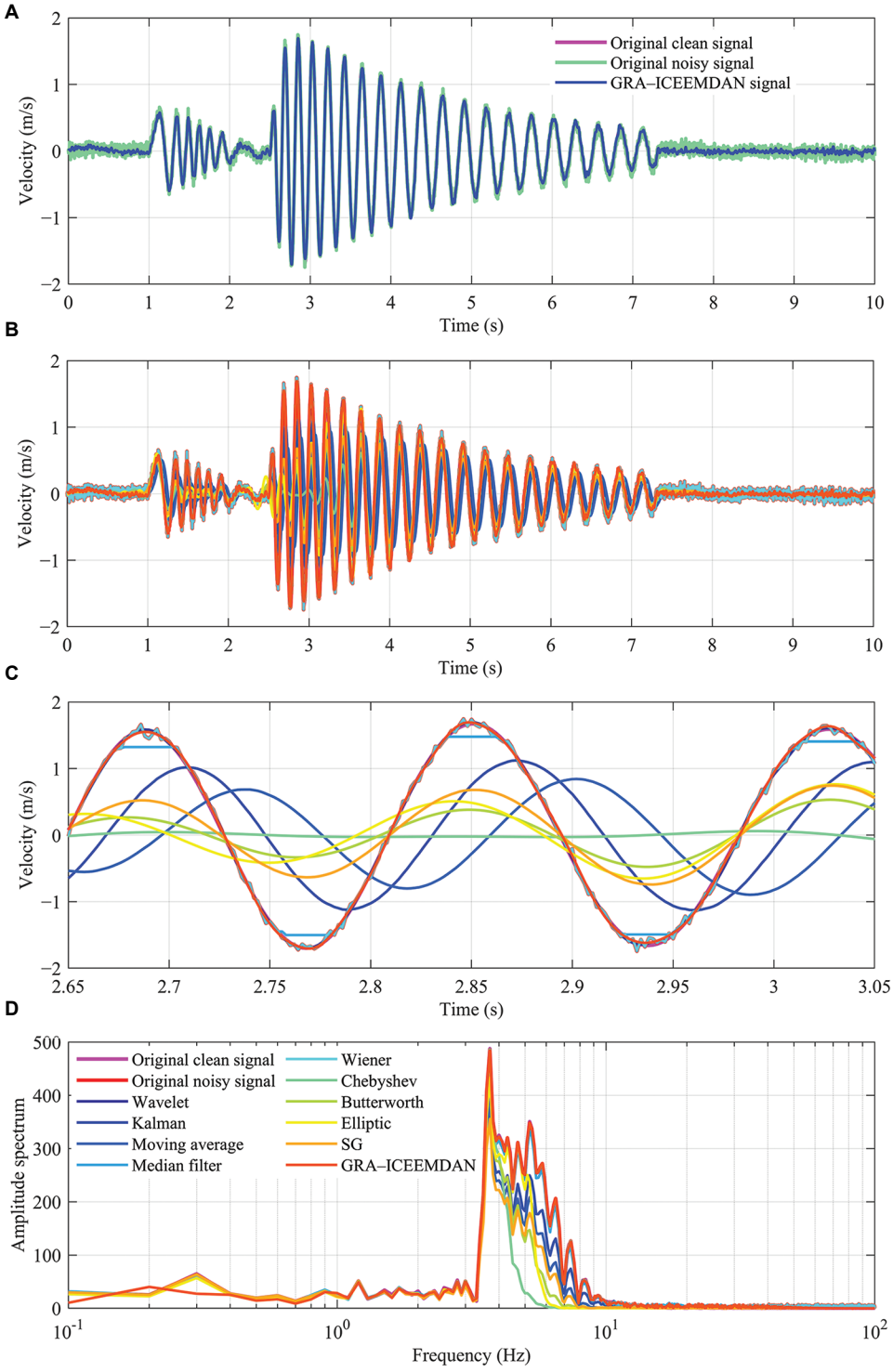

Figure 3. Comparison of waveforms before and after noise reduction for simulated seismic signals under different noise reduction models. Comparison of (A) denoising results between the original noisy signal and GRA–ICEEMDAN, (B) results from multiple noise reduction methods, (C) localized amplified waveforms from multiple noise reduction models, and (D) results from multiple denoising models (0.1–100 Hz).
Abbreviations: GRA: Grey relational analysis; ICEEMDAN: Improved complete ensemble empirical mode decomposition with adaptive noise signal denoising; SG: Savitzky–Golay.

ranges of 0.1–0.4 Hz and 3.5–10 Hz. Spectral consistency in other regions generally remained at an acceptable level. Therefore, when processing complex waveforms, such as simulated seismic waves, most models produced noise rejection misjudgments, failing to accurately locate the phase position and main peak scale of the effective signal. This leads to significant misjudgments in both the time domain and frequency domain. The excellent performance of the wavelet and GRA–ICEEMDAN models on simulated waveforms offers new insights and application prospects for seismic data processing. Further evaluation of their applicability scope requires incorporating comparative analysis with real seismic signals.

Figure 4 presents bar charts comparing denoising metrics for simulated seismic signals across different denoising models. This visualization clearly reveals the performance differences among models in both overall metrics and specific indicators. The combined score bars for the GRA–ICEEMDAN and wavelet models are tied at the highest position, clearly demonstrating their leading advantage in overall denoising performance. Further examination of the sub-metric bar charts revealed that despite their identical total scores, their performance characteristics diverged. The GRA–ICEEMDAN model maintained high levels across SNR, correlation, frequency similarity, and energy retention, forming a relatively balanced "performance spectrum". However, its bar height for noise suppression rate is significantly lower than that of other high-scoring models. This apparent "weakness" aligns with its algorithm's restrained approach to noise removal—prioritizing signal fidelity over aggressive noise elimination to prevent excessive distortion.

In contrast, the composite score bar for the moving average and Chebyshev models clearly ranked in the lowest tier. Their sub-metric bar charts exhibited a distinctly polarized pattern: The bar for noise suppression rate was exceptionally prominent, nearly reaching full value, while the bars for SNR and energy retention rate were severely depressed. This stark contrast in the bar charts directly visualizes the flaw of "excessive denoising" severely damaging the effective signal, explaining why these models rank at the bottom. The bar shapes for Butterworth, elliptic, Savitzky–Golay, Wiener, and Kalman models also exhibited similar imbalances, albeit to varying degrees. These bar charts clearly revealed the distribution characteristics of performance differences among models and their strengths and weaknesses across different dimensions, enhancing the objectivity and persuasiveness of the discussion on denoising model results. Detailed denoising evaluation metric data are fully presented in Table 4.

Based on the overall score ranking results (GRA–ICEEMDAN=Wavelet>Median filter>Wiener>Savitzky–Golay>Elliptic filter>Butterworth filter>Kalman filter>Chebyshev filter>Moving average), it can be observed that the GRA–ICEEMDAN model and wavelet denoising model demonstrated superior overall noise suppression performance, both achieving a perfect score of 100 (out of 100). Their performances across individual evaluation metrics were also relatively balanced. Specifically, the GRA–ICEEMDAN model's sub-metric scores were 24.0049 dB for SNR, 87.9105% for noise suppression rate, 0.9946 for signal correlation, 99.7962% for frequency similarity, and 99.0641% for energy retention. Compared to the white noise power introduced into the clean signal (20 dB), it achieved an improvement of 4.0049 dB. The entire denoising process took 3.7754 s to compute. Each metric contributed equally to the overall calculation. Among the 10 denoising models, it ranked second, eighth, fourth, and second in SNR, noise

Table 4. Comparison of the denoising effects of the models based on simulated denoised data

Denoising model	SNR (db)	Noise suppression ratio (%)	Correlation	Frequency similarity (%)	Energy retention (%)	Overall score
Wavelet	30.5713	97.2009	0.9952	99.8684	98.9768	100
Kalman filter	3.8652	99.3746	0.7650	99.4674	55.6142	71.7661
Moving average	−1.0326	99.8781	0.1233	97.7523	42.6740	52.2340
Median filter	23.3959	81.6674	0.9948	99.8196	92.3022	98.1086
Wiener filter	20.0868	2.0009	0.9999	99.9999	99.8454	80.4561
Chebyshev filter	3.0365	99.9982	0.7163	71.7636	34.6873	62.1236
Butterworth filter	5.8201	99.9998	0.8871	89.0363	42.0791	72.5777
Elliptic filter	6.3841	99.9998	0.8820	88.5631	57.0188	74.7498
Savitzky–Golay	6.7753	99.9045	0.9591	96.3679	34.4964	75.6013
GRA–ICEEMDAN	24.0049	87.9105	0.9946	99.7962	99.0641	100

Abbreviations: GRA: Grey relational analysis; ICEEMDAN: Improved complete ensemble empirical mode decomposition with adaptive noise signal denoising; SNR: Signal-to-noise ratio.

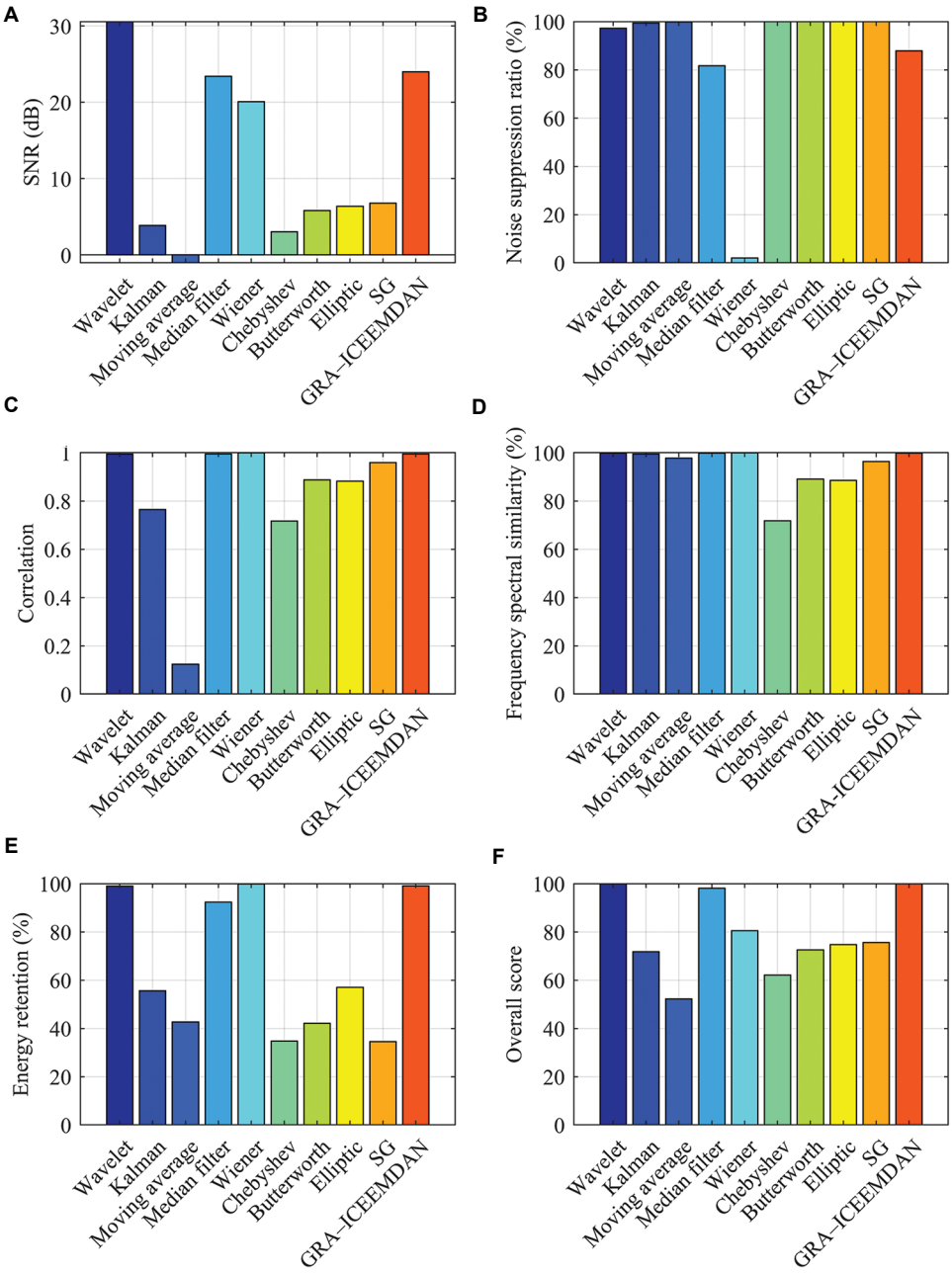

Figure 4. Bar chart comparison of noise reduction metrics for simulated seismic signals under different noise reduction models. (A) Signal-to-noise ratio (SNR) improvement. (B) Noise suppression ratio. (C) Correlation. (D) Frequency spectral similarity. (E) Energy retention. (F) Overall score.
Abbreviations: GRA: Grey relational analysis; ICEEMDAN: Improved complete ensemble empirical mode decomposition with adaptive noise signal denoising; SG: Savitzky–Golay.

suppression rate, signal correlation, frequency spectrum similarity, and energy retention, respectively, with most individual metrics ranking highly. However, its ranking for noise suppression ratio (87.9105%) was low. This is because the GRA–ICEEMDAN model automatically balances the relationship between main frequency energy retention, waveform consistency, and noise suppression. It controls noise removal within manageable limits to prevent energy leakage or severe amplitude distortion.

Some models exhibited poor overall noise reduction performance, such as the moving average and Chebyshev models, which demonstrate subpar denoising capabilities (overall score < 65). Their post-denoising performance and waveform characteristics differed significantly from

those of other models. Furthermore, their performance metrics (noise suppression ratio of 99.8781% and 99.9982%, respectively) confirmed that these models suffer from excessive denoising, rendering them incapable of accurately assessing noise suppression levels. (SNR < 4 dB, Energy retention < 45%). Consequently, they lack competitiveness in overall score rankings. Models, such as Butterworth, elliptic, Savitzky–Golay, Wiener, and Kalman exhibited similar noise reduction flaws, all displaying varying degrees of excessive denoising. This directly leads to severe distortion of the original waveform and phase confusion, imposing certain limitations on their application in reliable seismic monitoring and geophysical exploration projects.

4. Experiment and analysis of nodal seismograph signal denoising

The IGU-16HR nodal seismograph is a highly representative wireless and velocity-type intelligent instrument in the fields of geophysical exploration and seismic monitoring. It possesses advantages such as low cost, long battery life, small size, and rapid deployment. It can be equipped with various tools, including a mobile deployment terminal, a smart app, a charging box, a data download box, and data pre-processing desktop software, to enhance its field observation capabilities. The main performance parameters of the 5 Hz instrument are support for continuous data acquisition for 35 days, distortion less than 0.1%, spurious frequency greater than 170 Hz, open-circuit intrinsic voltage sensitivity of 80 V/m/s, sampling interval support of 0.25–4 ms, IP68 waterproof rating, built-in 206.5 Hz anti-aliasing filter and 1–10 Hz DC blocking filter, system dynamic range of 145 dB, and frequency response of 0–1,652 Hz. Given the superior performance of the IGU-16HR nodal seismograph, this study mainly utilizes data recorded by this model to conduct various denoising experiments and analyses.

The GRA–ICEEMDAN denoising experimental data mainly came from the Ms 3.2 earthquake event recorded on June 27, 2025, in Lichuan, Hubei, China, by a single-component SmartSolo IGU-16HR nodal seismograph, and the geopulsation environmental excitation event recorded on May 31, 2025, at a seismic station on the campus of Wuhan University in Wuhan, Hubei. The sampling rates were 500 Hz and 1,000 Hz, respectively. The former signal successfully recorded the S-coda wave of the earthquake event, and the latter signal successfully recorded the regular geopulsation information of the city at night. Experimental platform and algorithm parameters: The simulation platform used was MATLAB 2024b, and the signal length was 10 s. The noise intensity, number of ensembles, and maximum number of iterations for ICEEMDAN decomposition were 0.2, 3, and 3,600, respectively. The similarity tolerance threshold for sample entropy was the product of 0.15 and the signal standard deviation.

4.1. Denoising experiment of S-coda waves recorded by nodal seismograph

First, GRA–ICEEMDAN denoising analysis was performed on the S-coda waves of natural seismic events recorded by node seismometers. The signal sampling rate was 500 Hz, and the experimental data duration was 10 s. The GRA analysis process data are shown in Tables 5-7, the signal decomposition results are shown in Figure 5, and the denoising results under various models are shown in Table 8 and Figures 6-8.

Figure 5 shows the schematic diagram of the eight IMF components obtained by decomposing the seismic signal recorded by the node seismometer using ICEEMDAN. From Figure 5, it can be observed that IMF_1 to IMF_4 contained substantial noise with overall minimal amplitudes, exhibiting generally high oscillation frequencies around the zero-time point throughout the entire time domain.

Table 5. Characteristic parameter values of each IMF in the S-coda waves of seismic events recorded by nodal seismographs

IMF	Correlation coefficient	Sample entropy	CS	R^2	JSD	RMSE	MAE	MAPE	Adj-R^2	MI
IMF_1	0.3213	0.3936	0.1564	−3.1168	0.3256	1.3282e−07	1.1774e−07	1.2357	0.1030	0.7722
IMF_2	0.3111	0.9169	0.1541	−3.1244	0.2510	1.3294e−07	1.1777e−07	1.1729	0.0966	0.8721
IMF_3	0.0921	0.6396	0.0420	−3.2106	0.2842	1.3433e−07	1.1825e−07	1.0660	0.0082	0.8558
IMF_4	0.0100	0.5480	0.0132	−3.2174	0.2931	1.3444e−07	1.1829e−07	1.0093	−9.9532e−05	0.8784
IMF_5	0.0766	0.1629	0.0338	−3.2137	0.2787	1.3438e−07	1.1835e−07	1.0232	0.0056	0.8792
IMF_6	0.4057	0.0372	0.0083	−3.2357	0.2753	1.3473e−07	1.1997e−07	1.3947	0.1644	0.8835
IMF_7	0.5731	0.0138	0.2251	−3.0392	0.1844	1.3157e−07	1.2082e−07	1.8793	0.3284	0.9049
IMF_8	0.5723	0.0031	0.9160	0.3101	0.0348	5.4372e−08	4.6263e−08	1.9774	0.3274	0.9099

Abbreviations: Adj-R^2: Adjusted coefficient of determination; CS: Cosine similarity; IMF: Intrinsic mode function; JSD: Jensen–Shannon divergence; MAE: Mean absolute error; MAPE: Mean absolute percentage error; MI: Mutual information; R^2: Coefficient of determination; RMSE: Root mean square error.

Table 6. Comparison and reference series values of each IMF for S-coda waves of seismic events recorded by nodal seismographs

Index	The IMF evaluated								Ideal IMF
	IMF_1	IMF_2	IMF_3	IMF_4	IMF_5	IMF_6	IMF_7	IMF_8	
Correlation coefficient	0.5527	0.5346	0.14579	0	0.1182	0.7026	1	0.9984	1
Sample entropy	0.5727	0	0.3034	0.4036	0.8250	0.9626	0.9882	1	1
CS	0.1631	0.1606	0.0371	0.0053	0.0280	0	0.2388	1	1
R^2	0.0335	0.0313	0.0070	0.0051	0.0062	0	0.0554	1	1
JSD	0	0.2565	0.1424	0.1118	0.1613	0.1731	0.4855	1	1
RMSE	0.0237	0.0221	0.0049	0.0036	0.0043	0	0.0393	1	1
MAE	0.0413	0.0408	0.0344	0.0339	0.0332	0.0114	0	1	1
MAPE	0.7661	0.8310	0.9414	1	0.9856	0.6018	0.1013	0	1
Adj-R^2	0.3140	0.2944	0.0255	0	0.0175	0.5008	1	0.9969	1
MI	0	0.7251	0.6073	0.7708	0.7768	0.8085	0.9638	1	1

Abbreviations: Adj-R^2: Adjusted coefficient of determination; CS: Cosine similarity; IMF: Intrinsic mode function; JSD: Jensen–Shannon divergence; MAE: Mean absolute error; MAPE: Mean absolute percentage error; MI: Mutual information; R^2: Coefficient of determination; RMSE: Root mean square error.

Table 7. Grey relational analysis correlation coefficients and correlation values of each IMF in the S-coda waves of seismic events recorded by nodal seismographs

Evaluation indicators	The IMF evaluated							
	IMF_1	IMF_2	IMF_3	IMF_4	IMF_5	IMF_6	IMF_7	IMF_8
Correlation coefficient	0.5278	0.5179	0.3692	0.3333	0.3618	0.6270	1	0.9969
Sample entropy	0.5391	0.3333	0.4178	0.4560	0.7408	0.9304	0.9769	1
CS	0.3740	0.3733	0.3418	0.3345	0.3396	0.3333	0.3964	1
R^2	0.3409	0.3404	0.3349	0.3344	0.3347	0.3333	0.3461	1
JSD	0.3333	0.4021	0.3683	0.3601	0.3735	0.3768	0.4928	1
RMSE	0.3387	0.3383	0.3344	0.3341	0.3343	0.3333	0.3423	1
MAE	0.3427	0.3426	0.3411	0.3410	0.3408	0.3358	0.3333	1
MAPE	0.6813	0.7474	0.8951	1	0.9720	0.5567	0.3574	0.3333
Adj-R^2	0.4215	0.4147	0.3391	0.3333	0.3372	0.5004	1	0.9940
MI	0.3333	0.6452	0.5601	0.6857	0.6914	0.7230	0.9325	1
Correlation	0.4233	0.4455	0.4302	0.4512	0.4826	0.5050	0.6178	0.9324

Abbreviations: Adj-R^2: Adjusted coefficient of determination; CS: Cosine similarity; IMF: Intrinsic mode function; JSD: Jensen–Shannon divergence; MAE: Mean absolute error; MAPE: Mean absolute percentage error; MI: Mutual information; R^2: Coefficient of determination; RMSE: Root mean square error.

The curves of IMF_5 to IMF_8 demonstrated significantly smoother and more stable characteristics compared to IMF_1 to IMF_3, showing no concentration of energy, with amplitudes similarly remaining within a low range. IMF_7 exhibited high similarity to the original waveform, a similarity supported by objective assessment through COEFs or mutual information metrics. After obtaining the ICEEMDAN decomposition results for seismic event signals recorded by node seismometers (Figure 5), 10 characteristic index values were calculated for each IMF, as presented in Table 5.

Table 5 presents the evaluation metrics for each IMF component following the ICEEMDAN decomposition of node seismometer signals. It is evident that IMF_6 to IMF_8 exhibited significant differences from other IMF components across multiple evaluation metrics, such as sample entropy, Adj-R^2, COEF, and mutual information. Particularly, numerous eigenvalues of the IMF_8 component exhibited extreme contrasts in magnitude compared to other IMFs, while simultaneously presenting minimal values in metrics, such as RMSE and MAE, which express the absolute error between two signals.

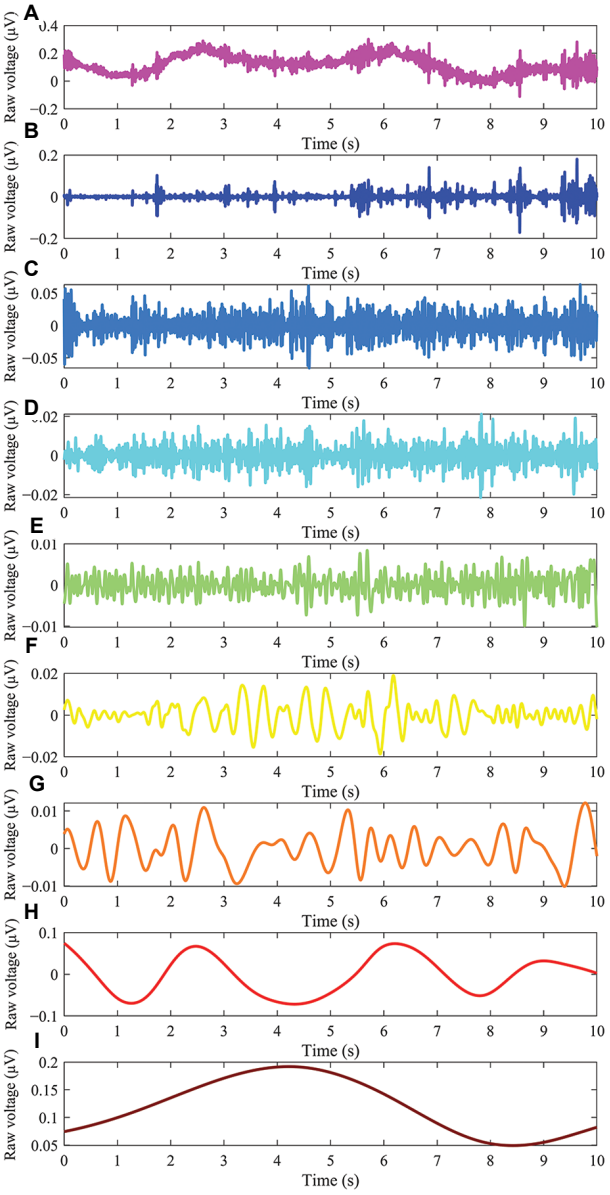

Figure 5. Schematic diagram of eight IMFs obtained by decomposing the S-coda wave of a seismic event recorded by a nodal seismograph using ICEEMDAN. (A) Original noisy signal. (B) IMF_1. (C) IMF_2. (D) IMF_3. (E) IMF_4. (F) IMF_5. (G) IMF_6. (H) IMF_7. (I) IMF_8.
Abbreviation: ICEEMDAN: Improved complete ensemble empirical mode decomposition with adaptive noise signal denoising; IMF: Intrinsic mode function.

The IMF quality evaluation metric matrix is derived from Table 5. After undergoing standardization, two-stage least squares/two-stage maximum difference calculation, grey relational coefficient calculation, subjective assignment of indicator weights, and IMF correlation analysis, the final quality ranking results for IMF components are presented in Tables 6 and 7. Table 6 shows the comparison sequences and reference sequence values for each IMF of the seismic event signal recorded by the node seismometer, while Table 7 presents the GRA COEFs and correlation values for each IMF of the seismic event signal recorded by the node seismometer.

The comparison and reference sequences in Table 6 can be used to construct the GRA COEFs between 10 evaluation indicators and each IMF (Table 7). Based on the balanced indicator weight vector {0.1,0.1,0.1,0.1,0.1,0.1,0.1,0.1,0.1,0.1} and the GRA COEFs, the grey weighted correlation degree of each IMF was obtained using the arithmetic average (Table 7).

The final GRA correlation ranking results are: IMF_8 > IMF_7 > IMF_6 > IMF_5 > IMF_4 > IMF_2 > IMF_3 > IMF_1, with GRA scores of 0.9324, 0.6178, 0.5050, 0.4826, 0.4512, 0.4455, 0.4302, and 0.4233, respectively. As shown in Table 7, among all intrinsic modal functions, IMF_8 exhibited the highest correlation (0.9324) with the ideal IMF and possessed the optimal COEF (value of 1) for seven indicators, proving its superiority over any other IMF. IMF_7 follows with two optimal COEFs, and IMF_4 with one optimal COEF. Therefore, the top four IMF rankings (IMF_8, IMF_7, IMF_6, IMF_5) were selected for linear reconstruction, with results shown in Figure 6.

To compare the GRA–ICEEMDAN model's superiority among similar signal denoising models, nine reference models—wavelet threshold denoising, median filter, Wiener filter, Savitzky–Golay filter, elliptic filter, Butterworth filter, Kalman filter, Chebyshev filter, and moving average filter— were used. The evaluation framework incorporated quantitative metrics across multiple dimensions, including SNR improvement, noise suppression ratio, correlation, frequency similarity, energy retention, and overall score. The denoising results for each model are also displayed in Figure 6.

Except for the wavelet and Wiener models, other models produced positive effects in seismic signal denoising, achieving a certain degree of smoothing and high time-frequency fidelity (Figure 6A, B, and D), though they exhibited notable differences in waveform processing. Due to the presence of strong and widely distributed high-frequency noise in natural seismic signals, the 0.5-s local magnification view (Figure 6C) revealed that Kalman filtering, median filtering, and the moving average model retained some characteristics of high-frequency noise, causing severe phase distortion. In contrast, models such as GRA–ICEEMDAN, elliptic, Savitzky–Golay, and Butterworth models demonstrated superior high-frequency noise suppression. Their local waveforms exhibited smoother, more stable trajectories aligned with the original signal's progression and clustered near the center of the high-frequency signal curve.

Table 8. Comparison of nodal seismograph signal denoising effects under different models

Denoising model	SNR improvement (db)	Noise suppression ratio (%)	Correlation	Frequency similarity (%)	Energy retention (%)	Overall score
Wavelet	0.1605	3.6695	0.9991	99.9874	99.8499	60.8449
Kalman filter	11.9065	94.2601	0.9284	99.0835	96.3058	88.4194
Moving average	19.1154	99.4890	0.9053	98.6071	96.0155	96.0596
Median filter	15.9871	98.1776	0.9090	98.7174	96.4511	92.8514
Wiener filter	0.0896	2.0616	0.9999	99.9998	99.9178	60.4854
Chebyshev filter	19.5434	99.8199	0.9113	98.5363	76.5784	93.2656
Butterworth filter	19.5087	99.7969	0.9115	98.5428	96.1673	96.6554
Elliptic filter	19.4585	99.8301	0.9114	98.5356	76.5227	93.1759
Savitzky–Golay	20.3431	99.7280	0.9115	98.6013	95.8684	97.4314
GRA–ICEEMDAN	20.8926	99.8741	0.9115	98.5325	95.9888	98.0180

Abbreviations: GRA: Grey relational analysis; ICEEMDAN: Improved complete ensemble empirical mode decomposition with adaptive noise signal denoising; SNR: Signal-to-noise ratio.

Models with limited denoising efficacy (e.g., wavelet and Wiener) yielded results nearly identical to the original noisy waveform (Figure 6A), indicating complete failure in noise suppression. Simultaneously, the spectral curves of models, such as elliptic and Butterworth exhibited a noticeable shift in the 0.1–0.7 Hz low-frequency range compared to other models (Figure 6D). This indicates their pronounced low-frequency noise suppression capability, which may play a crucial role in monitoring geomovements and solid tides.

Figure 7 compares the short-time Fourier transform (STFT) spectra of denoised seismic signals recorded by node seismometers under different denoising models. Before the experiment, STFT parameters were uniformly set to ensure comparability among models: Hamming window (256 points), 97.7% overlap, and 512-point Fourier transform. The STFT time–frequency spectrum of the original noisy signal exhibited typical noise contamination characteristics. Across the time axis (0–10 s) and frequency axis (0–100 Hz), the time–frequency energy distribution was diffuse and lacked a distinct structure (Figure 7A), with yellow and orange regions heavily contaminated by noise. Weak blue-highlighted impact structures were visible in the frequency range of 100–250 Hz. Similar spectral patterns were observed in models, such as wavelet, Kalman, moving average, and Wiener (Figure 7B, C, D, and F). The temporal characteristics of the seismic signal were clearly discernible in the STFT spectra of models such as Chebyshev, Butterworth, elliptic, Savitzky–Golay, and GRA–ICEEMDAN (Figure 7G-K), revealing multiple prominent peak contours of the seismic signal. The GRA–ICEEMDAN model uniformly exhibited numerous continuous bright bands around 500 Hz, with impact peak positions showing high amplitude matching to the original signal. In addition, models, such as the median filter exhibited varying degrees of excessive denoising, where the suppression process destroyed original signal details and generated severe artifacts (Figures 7B-E).

Figure 8 presents bar chart comparisons of denoising metrics for ground motion signals recorded by node seismometers under different denoising models. The bars visually illustrate the performance distribution of each model across the overall score and sub-metrics. Notably, the GRA–ICEEMDAN model exhibited significantly higher overall score bars than other models, highlighting its leading position in comprehensive noise suppression performance. This model also demonstrated superior column heights for the SNR improvement and noise suppression rate sub-metrics, confirming its outstanding denoising capability. However, its columns for frequency spectrum similarity and energy retention rate were relatively low, consistent with the model's adjustments to waveforms for removing high-frequency and environmental noise. Nevertheless, the bar chart indicates these metrics remained at high levels (e.g., frequency similarity > 98%, energy retention > 95%).

In contrast, the wavelet and Wiener models' composite score bars were positioned at the lowest level. Yet, their bars for signal correlation, frequency similarity, and energy retention approached or reached the top, starkly contrasting their extremely low bars for SNR improvement and noise suppression rate. This visually reveals these models' severe deficiencies in critical noise suppression metrics, leading to their disadvantageous overall ranking. The multi-subgraph visualization of the bar chart provides an intuitive ranking of each sub-metric in the denoising evaluation. It also clearly reveals the

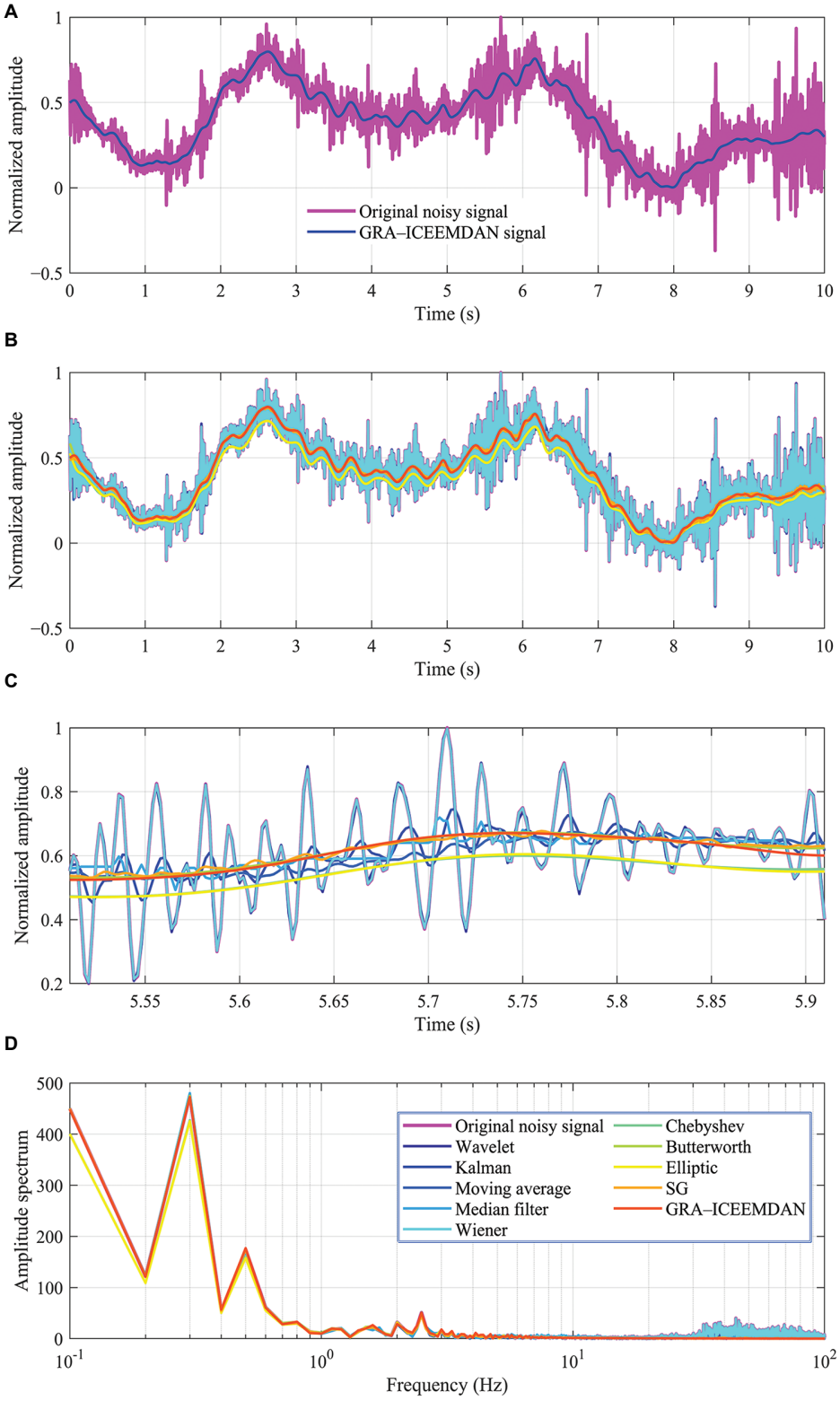

Figure 6. Comparison of waveforms for seismic signal denoising results from node seismometers under different denoising models. Comparison of (A) denoising results between the original noisy signal and GRA–ICEEMDAN, (B) results from multiple noise reduction methods, (C) localized amplified waveforms from multiple noise reduction models, and (D) results from multiple denoising models (0.1–100 Hz).

Abbreviations: GRA: Grey relational analysis; ICEEMDAN: Improved complete ensemble empirical mode decomposition with adaptive noise signal denoising; SG: Savitzky–Golay.

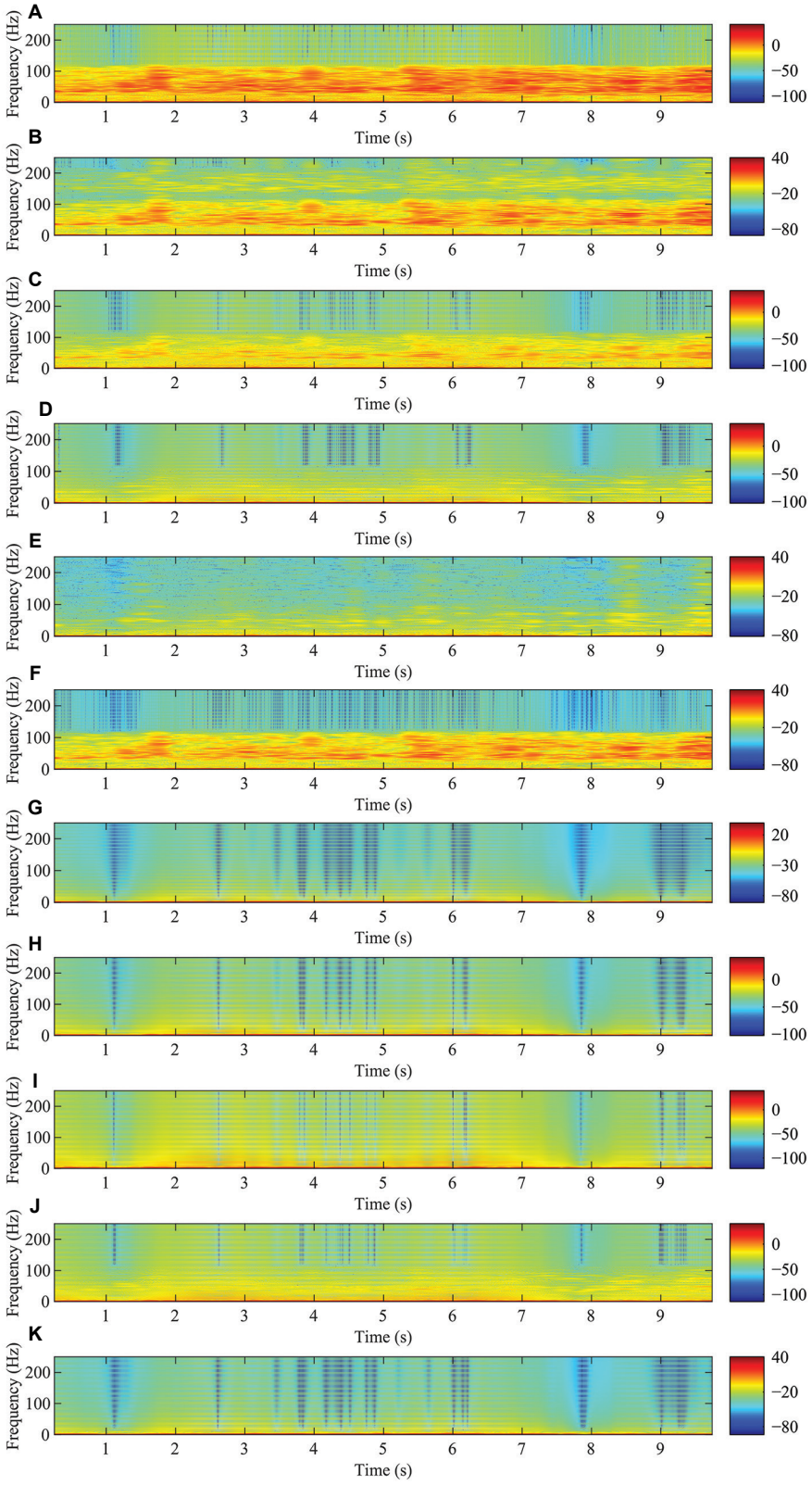

Figure 7. Comparison of short-time Fourier transform spectrograms for seismic signal denoising results from node seismometers under different denoising models. (A) Original noisy sound. (B) Wavelet. (C) Kalman. (D) Moving average. (E) Median filter. (F) Wiener. (G) Chebyshev. (H) Butterworth. (I) Elliptic. (J) Savitzky–Golay. (K) Grey relational analysis–improved complete ensemble empirical mode decomposition with adaptive noise signal denoising.

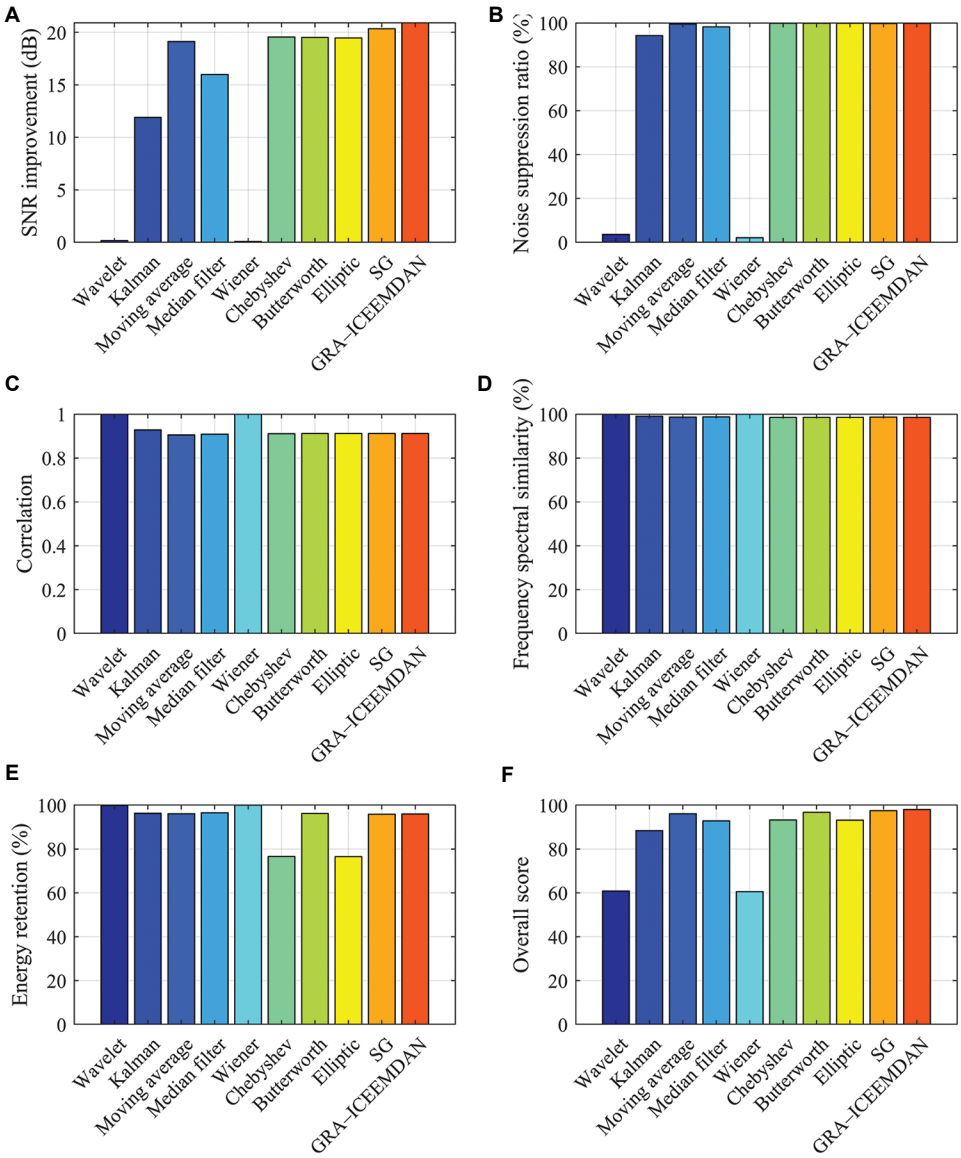

Figure 8. Comparison of short-time Fourier transform spectrograms for seismic signal denoising results from node seismometers under different denoising models. (A) Signal-to-noise ratio (SNR) improvement. (B) Noise suppression ratio. (C) Correlation. (D) Frequency spectral similarity. (E) Energy retention. (F) Overall score.

Abbreviations: GRA: Grey relational analysis; ICEEMDAN: Improved complete ensemble empirical mode decomposition with adaptive noise signal denoising; SG: Savitzky–Golay.

distribution characteristics of performance differences among models and their strengths and weaknesses across different dimensions, enhancing the objectivity and persuasiveness of the discussion on denoising model results. These detailed metric data are presented in Table 8.

Based on the ranking results by overall score (GRA–ICEEMDAN > Savitzky–Golay > Butterworth filter > Moving average > Chebyshev filter > Elliptic filter > Median filter > Kalman filter > Wavelet > Wiener), the GRA–ICEEMDAN model demonstrated superior overall noise suppression performance with an overall score of 98.0180 (out of 100). Its sub-indicator scores, SNR improvement, noise suppression rate, signal correlation, frequency spectrum similarity, and energy retention rate were 20.892 6 dB, 99.8741%, 0.9115, 98.5325%, and 95.9888%, respectively. All indicators were weighted equally, with a computation time of 3.6484 s. The model also demonstrated balanced performance across individual evaluation metrics, ranking first, first, fourth,

tenth, and seventh in SNR, noise suppression rate, signal correlation, frequency spectrum similarity, and energy retention, respectively, among the 10 denoising models. Most individual metrics were placed within the middle or higher tiers of the ranking cohort. The lower rankings in frequency similarity (98.5325%) and energy retention (95.9888%) stemmed from the GRA–ICEEMDAN model's extensive adjustments to the waveform shape. This approach effectively removed high-frequency components and most environmental noise from the original noisy signal, while still achieving over 98% restoration in the frequency domain.

Some models exhibited poor overall denoising performance, such as the wavelet and Wiener models (overall score < 65), showing significant differences compared to other models. Although wavelet demonstrated outstanding results in certain evaluation metrics (correlation=0.9991, frequency similarity = 99.9874%, energy retention = 99.8499%), with extremely high similarity between pre- and post-denoising results in both time-domain and frequency-domain signals, it failed to accurately assess noise suppression levels (SNR improvement = 0.1605 dB, noise suppression ratio=3.6695%), rendering it uncompetitive in overall rankings. This highlights algorithmic limitations in practical applications, with the Wiener model exhibiting similar deficiencies in noise reduction effectiveness.

However, conducting GRA–ICEEMDAN denoising experiments on natural earthquake events cannot meet the goal of verifying the universality of the new model's denoising. Further denoising experiments on other types of signals recorded by nodal seismographs are needed, which will be analyzed in Section 4.2.

4.2. Denoising experiment of ground pulsation signals recorded by node seismometers

The GRA–ICEEMDAN denoising analysis was performed on the unidirectional signal recorded by the node seismometer for the ground pulsation signal. The signal sampling rate was 1,000 Hz. The signal decomposition results, GRA calculation process data, and denoising statistical results are shown in Tables 9-12 and Figures 9-12.

Figure 9 illustrates the nine IMF components obtained through ICEEMDAN decomposition of the ground pulsation signal recorded by the node seismometer. Table 9 lists the characteristic parameter values for each IMF component after ICEEMDAN decomposition. IMF_1 to IMF_4, obtained from decomposing the noisy signal, all exhibited significant oscillations at relatively high frequencies with small amplitudes. Correspondingly, their sample entropy values all exceeded 0.50, their COEFs were all less than 0.15, and R^2 values clustered around 0.01. These waveform characteristics differ markedly from other IMFs, aligning more closely with the random oscillatory nature of environmental noise. Consequently, these components can be identified as system noise requiring removal. The waveform complexity and zero-crossing frequency of IMF_5 and IMF_6 fell between those of preceding and succeeding IMFs. Their metric values also spanned the range between maximum and minimum values. Whether to include them in the final signal reconstruction requires subsequent ranking and differentiation using the correlation scores from the GRA model. IMF_7–IMF_9 exhibited smoother waveforms with fewer spikes and pronounced low-frequency characteristics (sample entropy < 0.006, MSE > 0.2), closely resembling standard sine wave curves. These are presumed to be effective components of the original signal. Notably, IMF_7 exhibited high consistency with the

Table 9. Characteristic parameter values of each IMF after ICEEMDAN decomposition of the ground pulsation signals recorded by nodal seismographs

IMF	Correlation coefficient	Sample Entropy	CS	R^2	JSD	RMSE	MAE	MAPE	Adj-R^2	MI
IMF_1	0.1028	1.9775	0.1029	0.0101	0.3769	77.9736	68.8421	1.0463e+16	0.0104	0.6487
IMF_2	0.1321	1.3067	0.1321	0.0161	0.3682	77.7401	68.7084	1.2036e+16	0.0173	0.6759
IMF_3	0.1205	0.6596	0.1206	0.0137	0.3659	77.8339	68.7215	1.3078e+16	0.0144	0.6927
IMF_4	0.1026	0.5525	0.1026	0.0100	0.3630	77.9782	68.7346	1.1521e+16	0.0104	0.6918
IMF_5	0.1502	0.2163	0.1503	0.0214	0.3657	77.5308	68.5060	1.6317e+16	0.0224	0.6999
IMF_6	0.1681	0.0798	0.1679	0.0260	0.3238	77.3465	68.5524	1.3125e+16	0.0281	0.7072
IMF_7	0.9209	0.0059	0.9154	0.8213	0.0414	33.1294	26.5277	3.1722e+16	0.8480	0.7182
IMF_8	0.7955	0.0046	0.7810	0.2680	0.1198	67.0541	57.5983	1.6269e+16	0.6328	0.7166
IMF_9	0.2771	0.0027	0.2272	0.0500	0.4571	76.3866	66.3474	2.1118e+16	0.0767	0.7085

Abbreviations: Adj-R^2: Adjusted coefficient of determination; CS: Cosine similarity; ICEEMDAN: Improved complete ensemble empirical mode decomposition with adaptive noise signal denoising; IMF: Intrinsic mode function; JSD: Jensen–Shannon divergence; MAE: Mean absolute error; MAPE: Mean absolute percentage error; MI: Mutual information; R^2: Coefficient of determination; RMSE: Root mean square error.

original signal (COEF = 0.9209, R^2 = 0.8213, JSD = 0.0414, Adj-R^2 = 0.8480, MAE = 26.5277), and can be regarded as the primary noise-free component extracted from the original noisy signal.

After obtaining the ICEEMDAN decomposition results of the ground pulsation signals recorded by the nodal seismographs (Figure 9), the 10 characteristic index values of each of the above IMFs were calculated, as shown in Table 9.

The IMF quality evaluation indicator matrix was derived from Table 9. After undergoing necessary processing steps—including normalization, two-stage least squares/maximum differences calculation, grey relational coefficient computation, subjective assignment of indicator weights, and IMF correlation analysis—the final quality ranking results for IMF components were obtained. The specific calculation results are shown in Tables 10 and 11. Table 10 presents the comparative sequences and reference sequence values for each IMF of the ground pulsation signals recorded by the node seismometer, while Table 11 displays the GRA COEFs and correlation values for each IMF of the ground pulsation signals recorded by the node seismometer.

Table 10. Comparison and reference series values of ground vibration signals recorded by nodal seismographs for each IMF

Index	The IMF evaluated									Ideal IMF
	IMF_1	IMF_2	IMF_3	IMF_4	IMF_5	IMF_6	IMF_7	IMF_8	IMF_9	
Correlation coefficient	0.0002	0.0360	0.0218	0	0.0581	0.0801	1	0.8467	0.2133	1
Sample entropy	0	0.3396	0.6673	0.7215	0.8918	0.9609	0.9983	0.9990	1	1
CS	0.0004	0.0363	0.0221	0	0.0586	0.0803	1	0.8346	0.1532	1
R^2	0.0001	0.0074	0.0045	0	0.0139	0.0196	1	0.3179	0.0493	1
JSD	0.1927	0.2136	0.2191	0.2260	0.2195	0.3205	1	0.8113	0	1
RMSE	0.0001	0.0053	0.0032	0	0.0099	0.0140	1	0.2435	0.0354	1
MAE	0	0.0031	0.0028	0.0025	0.0079	0.0068	1	0.2657	0.0589	1
MAPE	1	0.9260	0.8770	0.9502	0.7246	0.8747	0	0.7269	0.4987	1
Adj-R^2	0.0005	0.0082	0.0047	0	0.0143	0.0212	1	0.7429	0.0791	1
MI	0	0.3917	0.6337	0.6207	0.7369	0.8419	1	0.9780	0.8613	1

Abbreviations: Adj-R^2: Adjusted coefficient of determination; CS: Cosine similarity; IMF: Intrinsic mode function; JSD: Jensen–Shannon divergence; MAE: Mean absolute error; MAPE: Mean absolute percentage error; MI: Mutual information; R^2: Coefficient of determination; RMSE: Root mean square error.

Table 11. GRA correlation coefficients and correlation values of each IMF in the ground pulsation signals recorded by nodal seismographs

Evaluation indicators	The IMFs evaluated								
	IMF_1	IMF_2	IMF_3	IMF_4	IMF_5	IMF_6	IMF_7	IMF_8	IMF_9
Correlation coefficient	0.3333	0.3415	0.3382	0.3333	0.3467	0.3521	1	0.7653	0.3885
Sample entropy	0.3333	0.4309	0.6004	0.6423	0.8221	0.9275	0.9966	0.9980	1
CS	0.3334	0.3416	0.3383	0.3333	0.3468	0.3521	1	0.7515	0.3712
R^2	0.3333	0.3349	0.3343	0.3333	0.3364	0.3377	1	0.4229	0.3446
JSD	0.3824	0.3887	0.3903	0.3924	0.3904	0.4239	1	0.7260	0.3333
RMSE	0.3333	0.3345	0.3340	0.3333	0.3355	0.3364	1	0.3979	0.3414
MAE	0.3333	0.3340	0.3339	0.3338	0.3351	0.3348	1	0.4050	0.3469
MAPE	1	0.8711	0.8025	0.9094	0.6448	0.7997	0.3333	0.6467	0.4993
Adj-R^2	0.3333	0.3351	0.3343	0.3333	0.3365	0.3381	1	0.6604	0.3519
Mutual Information	0.3333	0.4511	0.5772	0.5686	0.6552	0.7597	1	0.9579	0.7829
Correlation	0.4049	0.4164	0.4384	0.4513	0.4550	0.4963	0.9330	0.6732	0.4760

Abbreviations: Adj-R^2: Adjusted coefficient of determination; CS: Cosine similarity; IMF: Intrinsic mode function; JSD: Jensen–Shannon divergence; MAE: Mean absolute error; MAPE: Mean absolute percentage error; MI: Mutual information; R^2: Coefficient of determination; RMSE: Root mean square error.

Table 12. Comparison of nodal seismograph signal denoising effects under different models

Denoising model	SNR improvement (db)	Noise suppression ratio (%)	Correlation	Frequency similarity (%)	Energy retention (%)	Overall score
Wavelet	1.3157	25.4934	0.9977	99.9124	98.9379	66.1399
Kalman filter	10.8861	90.7295	0.9790	99.2136	95.8323	87.6389
Moving average	14.7322	95.4371	0.9552	98.4321	94.4711	91.5354
Median filter	14.1609	95.2443	0.9770	98.9580	95.0623	91.5796
Wiener filter	0.0759	1.6942	0.9999	99.9999	99.9272	60.4002
Chebyshev filter	16.1413	96.8667	0.9697	98.5302	75.7184	90.3033
Butterworth filter	16.2441	95.8946	0.9713	98.6158	93.9739	93.4027
Elliptic filter	16.1725	96.6147	0.9709	98.6003	75.7323	90.3244
Savitzky–Golay	15.1727	95.9182	0.9761	98.9484	94.6695	92.6313
GRA–ICEEMDAN	16.3523	96.3398	0.9774	98.8683	94.6693	93.9056

Abbreviations: GRA: Grey relational analysis; ICEEMDAN: Improved complete ensemble empirical mode decomposition with adaptive noise signal denoising; SNR: Signal-to-noise ratio.

The comparison and reference sequences in Table 10 can be used to construct the GRA COEFs between 10 evaluation indicators and each IMF (Table 11). Based on the balanced indicator weight vector {0.1,0.1,0.1,0.1,0.1,0.1 ,0.1,0.1,0.1,0.1,0.1} and the GRA COEFs, the grey weighted correlation degree of each IMF was obtained using the arithmetic average (Table 11).

IMF_7 achieved the highest COEF (value of 1) in 8 out of 10 indicators, indicating its most significant correlation with the original signal and the highest overall score (0.9330). IMF_1 and IMF_9 achieved the best results in MAPE and sample entropy indicators, respectively. The GRA comprehensive evaluation ranking is as follows: IMF_7 > IMF_8 (0.6732) > IMF_6 (0.4963) > IMF_9 (0.4760) > IMF_5 (0.4550) > IMF_4 (0.4513) > IMF_3 (0.4384) > IMF_2 (0.4164) > IMF_1 (0.4049). Although IMF_5, IMF_6, and IMF_8 did not achieve individual optimal values, their multiple COEFs exceeded 0.6, indicating high correlation with the signal and warranting retention. The remaining IMFs were discarded due to generally low correlation levels. The model selected the top five IMF components (IMF_7, IMF_8, IMF_6, IMF_9, IMF_5) for linear reconstruction, with the denoising results shown in Figure 10.

To evaluate the superiority of the GRA–ICEEMDAN model among comparable signal denoising methods, nine alternative models were selected for comparison: wavelet threshold denoising, median filter, Wiener filter, Savitzky–Golay filter, elliptic filter, Butterworth filter, Kalman filter, Chebyshev filter, and moving average filter. The evaluation framework incorporated multiple quantitative metrics across dimensions, including SNR improvement, noise suppression ratio, correlation, frequency similarity, energy retention, and overall score. The denoising results for each model are shown in Figure 10.

Except for the wavelet and Wiener models, other models produced positive effects in denoising geopotential signals, achieving a certain degree of smoothing and high time-frequency fidelity (Figure 10B and D), though with notable differences in waveform processing. Local magnified views revealed that the GRA–ICEEMDAN model exhibited superior phase consistency and better preservation of peak oscillation trends. Other models (e.g., moving average) directly filtered out local detailed features near peaks. The smoother curves obtained come at the cost of sacrificing more local effective components and phase information, which hinders the capture of signal details during subsequent data processing stages.

Models with limited denoising effectiveness (e.g., wavelet and Wiener) largely overlapped with the original noisy waveform (Figure 10A), indicating suboptimal noise suppression. In addition, the spectral curves of models, such as elliptic and Butterworth exhibited a certain degree of shift in the 0.1–0.4 Hz low-frequency range compared to other models (Figure 10D). This partially confirms that some models sacrifice local temporal features during denoising, thereby limiting their applicability in high-precision seismic monitoring and geophysical exploration.

Figure 11 compares the STFT spectra of denoised ground motion signals recorded by node seismometers under different denoising models. Before the experiment, STFT parameters were uniformly set to ensure comparability among models: Hamming window (256 points), 97.7% overlap, and 512-point Fourier transform. The STFT time–frequency spectrum of the original noisy signal exhibited

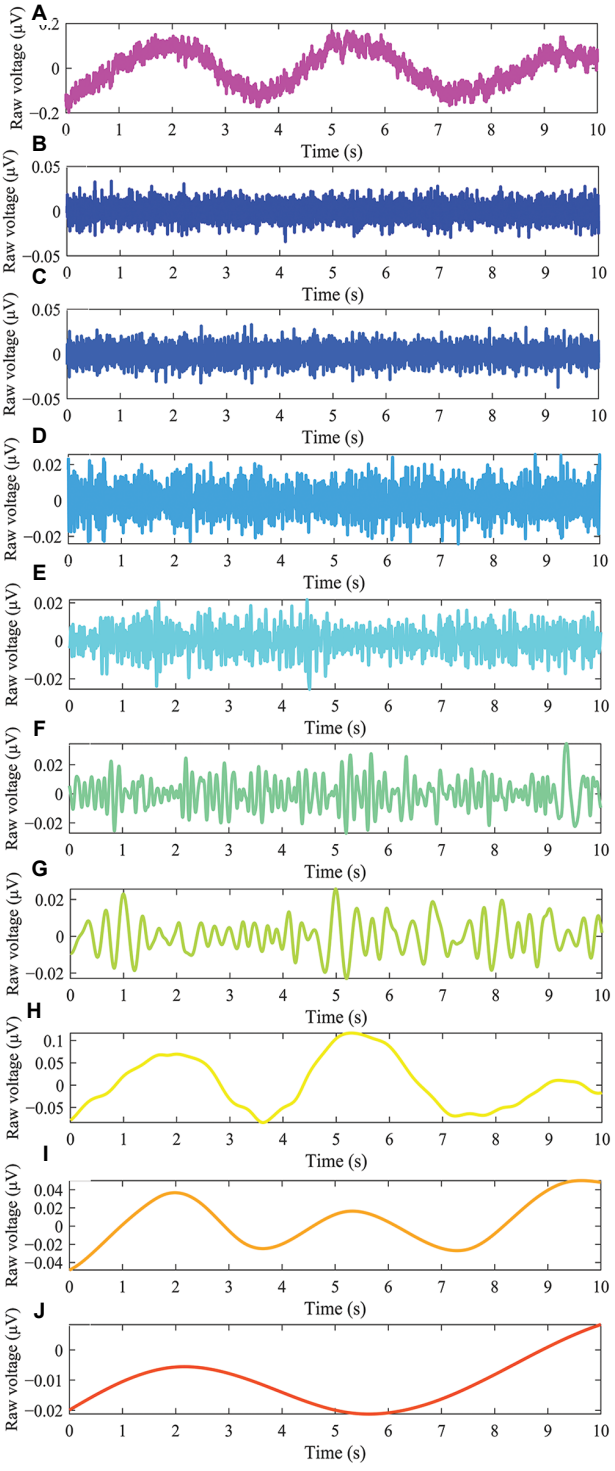

Figure 9. Results of the ground pulsation signals recorded by the nodal seismographs after ICEEMDAN decomposition. (A) Original noisy signal. (B) IMF_1. (C) IMF_2. (D) IMF_3. (E) IMF_4. (F) IMF_5. (G) IMF_6. (H) IMF_7. (I) IMF_8. (J) IMF_9.
Abbreviation: ICEEMDAN: Improved complete ensemble empirical mode decomposition with adaptive noise signal denoising; IMF: Intrinsic mode function.

typical noise contamination characteristics. Across the entire time axis (0–10 s) and frequency axis (0–400 Hz), the time–frequency energy distribution was diffuse and lacked a distinct structure (Figure 11A). In the region above the background noise (yellow and orange) at 400–500 Hz, the signal was severely contaminated by noise. Similar spectral patterns were observed for the wavelet model and Wiener model (Figure 11B and F). The temporal characteristics of the geopulse signal WERE clearly visible in the STFT spectra of models such as Chebyshev, Butterworth, elliptic, Savitzky–Golay, and GRA–ICEEMDAN (Figure 11G-K). Multiple prominent peak contours of the geodetic signal were discernible, while the GRA–ICEEMDAN model uniformly displayed numerous continuous bright bands at 500 Hz. The positions of impact peaks exhibited high amplitude, matching the original signal. Furthermore, models such as the median filter, the moving average, and the Kalman filter exhibited varying degrees of excessive noise reduction. The suppression process destroyed original signal details and produced severe artifacts (Figures 11B-E).

Figure 12 presents bar chart comparisons of denoising metrics for ground motion signals recorded by node seismometers under different denoising models. The bars visually illustrate the performance comparison across comprehensive scores and sub-metrics for each model. Notably, the GRA–ICEEMDAN model exhibited significantly higher comprehensive scores than other models, confirming its superior time–frequency balance across multiple evaluation metrics and its leading overall noise reduction performance. In contrast, the wavelet and Wiener models exhibited notably lower composite score bars, creating a stark contrast with their relatively high bars in certain metrics (e.g., signal correlation, frequency similarity). This further highlights their shortcomings in key noise suppression metrics (SNR improvement, noise suppression ratio), resulting in their disadvantageous position in the overall denoising evaluation. The multi-subgraph visualization of the bar chart provided an intuitive ranking of performance across sub-metrics in the denoising evaluation. It also clearly revealed the distribution characteristics of performance differences between models and their strengths and weaknesses across various dimensions, enhancing the objectivity and persuasiveness of the discussion on denoising model results. These detailed metric data are presented in Table 12.

Based on the overall score ranking (GRA–ICEEMDAN > Butterworth filter > Savitzky–Golay > Median filter > Moving average > Elliptic filter > Chebyshev filter > Kalman filter > Wavelet > Wiener), the GRA–

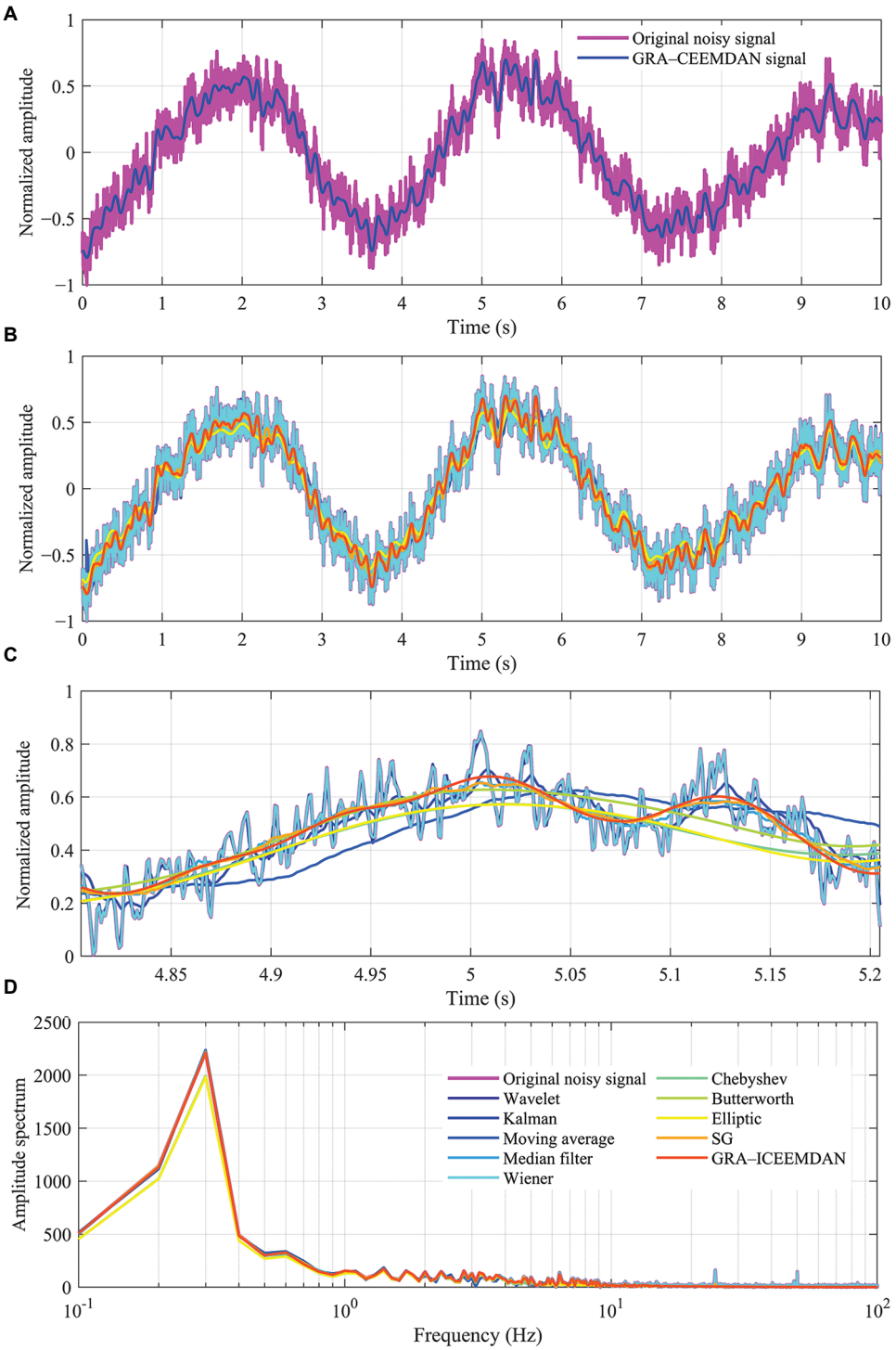

Figure 10. GRA–ICEEMDAN denoising results of ground vibration signals recorded by nodal seismographs. Comparison of (A) denoising results between the original noisy signal and GRA–ICEEMDAN, (B) results from multiple noise reduction methods, (C) localized amplified waveforms from multiple noise reduction models, and (D) results from multiple denoising models (0.1–100 Hz).

Abbreviations: GRA: Grey relational analysis; ICEEMDAN: Improved complete ensemble empirical mode decomposition with adaptive noise signal denoising; SG: Savitzky–Golay.

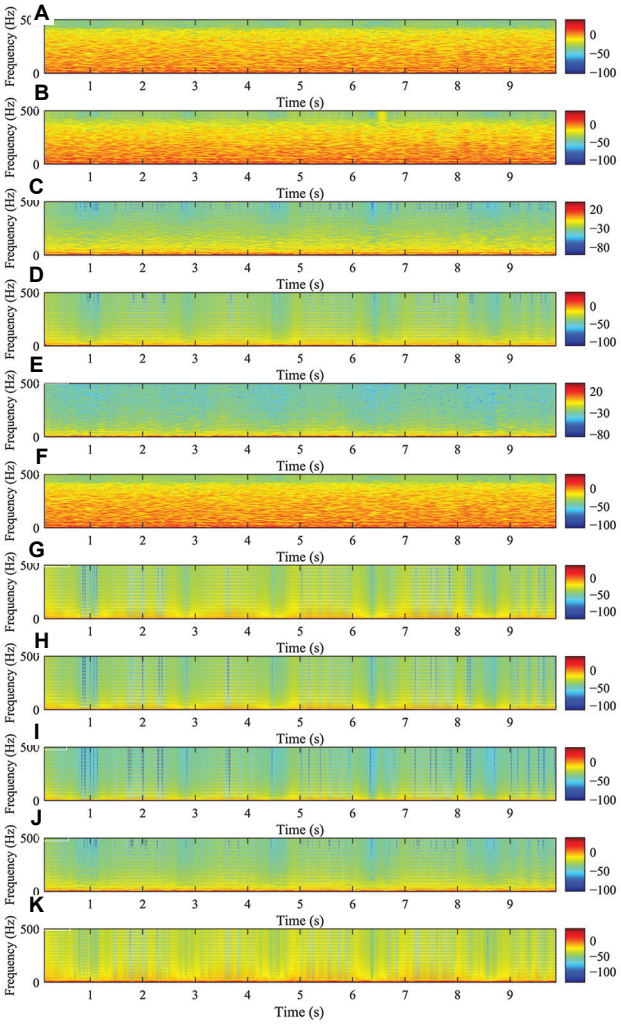

Figure 11. Comparison of short-time Fourier transform spectrograms for ground pulse signal denoising results from node seismometers under different denoising models. (A) Original noisy sound. (B) Wavelet. (C) Kalman. (D) Moving average. (E) Median filter. (F) Wiener. (G) Chebyshev. (H) Butterworth. (I) Elliptic. (J) Savitzky–Golay. (K) Grey relational analysis–improved complete ensemble empirical mode decomposition with adaptive noise signal denoising.

ICEEMDAN model demonstrated superior overall noise suppression performance. Its comprehensive score is 93.9056 (out of 100), with sub-metric scores as follows: SNR improvement: 16.3523 dB, noise suppression rate: 96.3398%, signal correlation: 0.9774, frequency spectrum similarity: 98.8683%, and energy retention rate: 94.6693%. The computation time was 12.9703 s. The model also demonstrated balanced performance across individual evaluation metrics, ranking first, third, fourth, sixth, and sixth in SNR, noise suppression rate, signal correlation, frequency spectrum similarity, and energy retention, respectively, among the 10 denoising models. All individual metrics were at or above the mid-range level in the ranking cohort, with no instances of poor "specialization" or concentrated performance.

Some models exhibited poor overall noise reduction performance, such as the wavelet and Wiener models (overall score <70), showing significant differences compared to other models. Although the wavelet model demonstrated outstanding results in certain evaluation metrics (correlation = 0.9977, frequency similarity = 99.9124%, energy retention = 98.9379%), with extremely high similarity between pre- and post-denoising results in both time-domain and frequency-domain signals, it failed to accurately assess noise suppression levels (SNR improvement = 1.3157 dB, noise suppression ratio = 25.4934%), rendering them uncompetitive in overall rankings. This highlights algorithmic shortcomings in practical applications, with the Wiener model exhibiting similar deficiencies.

5. Discussion

In addition to the SNR, the practical application effectiveness of denoising models requires consideration of more complex aspects, such as model robustness and algorithm robustness. To further evaluate the multi-round repeatable denoising robustness of the GRA–ICEEMDAN model, a cyclic denoising experiment was designed for nodal seismograph-recorded ground pulsation data with 20 rounds. The evaluation metrics for the denoising model included COEF, absolute difference of distribution entropy, reconstructed SNR, and MSE. Statistical indicators such as mean, standard deviation, range, and median were used to measure the consistency of the multi-round denoising results. The experimental results are shown in Figure 13 and Table 13.

Figure 13 shows the denoising results of 20 rounds of GRA-ICEEMDAN recorded ground pulsation signals by nodal seismographs, and Table 13 shows the statistical table of the denoising results of 20 rounds of nodal seismograph recorded ground pulsation signals. The denoising results of each time were highly correlated with the original waveform (mean >0.97, standard deviation <0.01), and no special cases of distortion or deformation occurred. The reconstructed SNR was greater than 10 dB, indicating that the GRA–ICEEMDAN model has a good random suppression effect on a large amount of environmental noise. The absolute value of the distribution entropy difference was all below 0.05, reflecting that the overall consistency of the waveform period before and after denoising by the GRA–ICEEMDAN model was high.

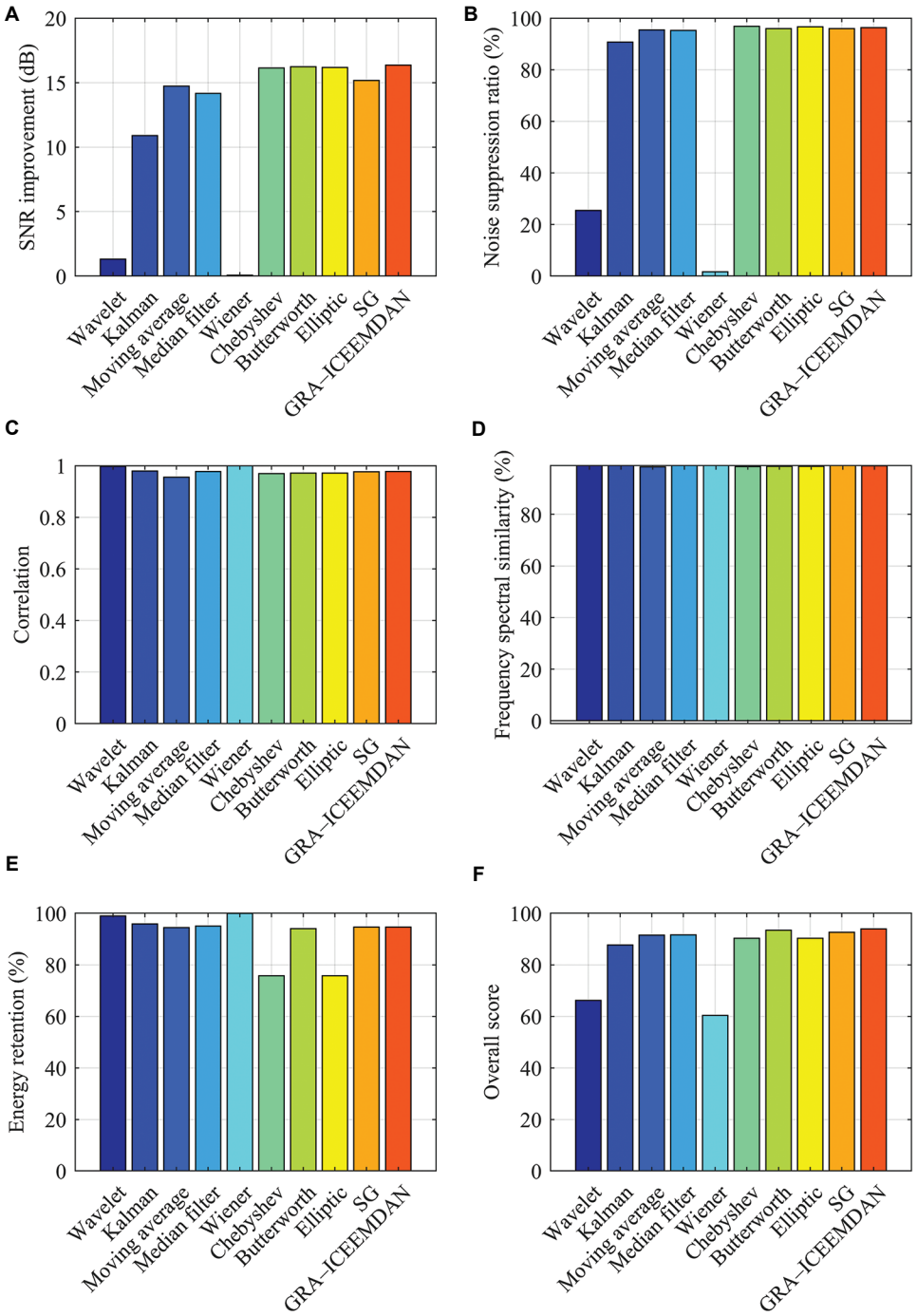

Figure 12. Bar chart comparison of denoising metrics for ground pulse signal recorded by node seismographs under different denoising models. (A) Signal-to-noise ratio (SNR) improvement. (B) Noise suppression ratio. (C) Correlation. (D) Frequency spectral similarity. (E) Energy retention. (F) Overall score.
Abbreviations: GRA: Grey relational analysis; ICEEMDAN: Improved complete ensemble empirical mode decomposition with adaptive noise signal denoising; SG: Savitzky–Golay.

The repeatability test results of the GRA–ICEEMDAN model in this section verified the stability of its denoising effect, improved the simulation test of the model, and largely demonstrated that the noise processing process of GRA combined with ICEEMDAN is feasible and reliable.

Table 13. Statistical table of 20 rounds of noise reduction results for ground pulsation signals recorded by nodal seismographs

Evaluation metrics	Mean	STD	Range	Median
Correlation coefficient	0.9720	0.0083	0.0323	0.9770
Mean square error	366.9937	115.6653	374.5581	288.7540
Absolute difference in distribution entropy	0.0336	0.0074	0.0308	0.0348
Reconstructed signal-to-noise ratio (dB)	12.4271	1.2874	3.8006	13.2809

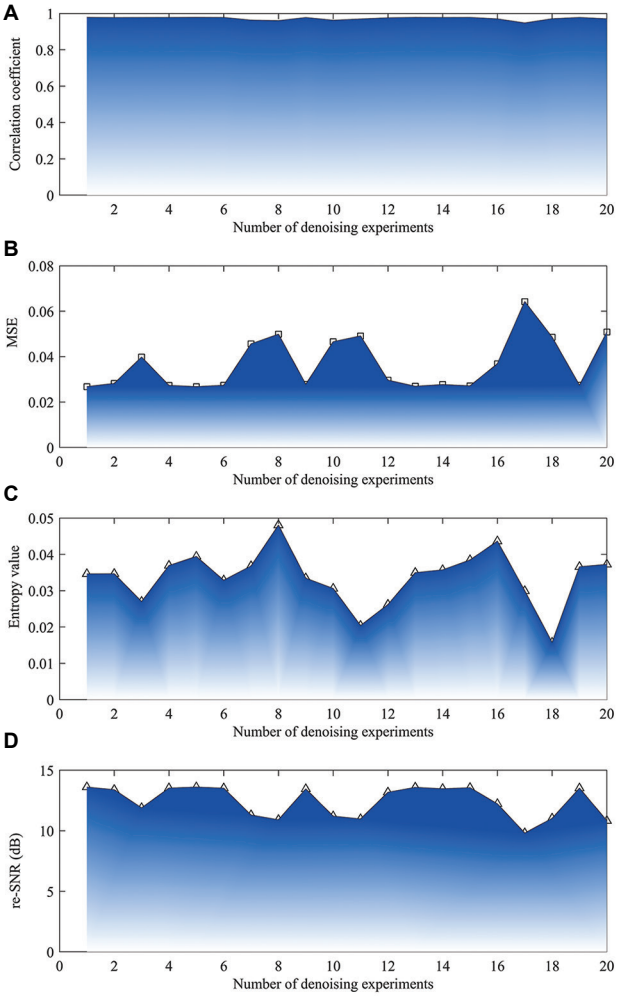

Figure 13. Twenty rounds of GRA–ICEEMDAN denoising results of ground pulsation signals recorded by nodal seismographs. (A) Correlation coefficient. (B) Mean square error. (C) Absolute value of the distribution entropy difference. (D) Reconstructed signal-to-noise ratio.
Abbreviations: GRA: Grey relational analysis; ICEEMDAN: Improved complete ensemble empirical mode decomposition with adaptive noise signal denoising.

6. Conclusion

This study proposed a joint denoising model based on ICEEMDAN and GRA to suppress random noise in various observation signals from nodal seismographs. Across systematic experiments on simulated signals, actual ground pulsation signals, and seismic event signals, as well as comparisons with traditional methods, such as Kalman filtering, Chebyshev filtering, Savitsky–Golay filtering, and Butterworth filtering, the following conclusions are drawn:

(i) Denoising effectiveness: This model achieved an excellent balance between preserving effective signals and suppressing random noise. In simulation experiments, it showed the greatest improvement in reconstructed SNR and the lowest MSE. In ground pulsation signal processing, it effectively smoothed the noise background and highlighted potential weak reflection information. In seismic event applications, it achieved the highest waveform fidelity for key phases, such as P-waves, effectively avoiding amplitude loss or phase distortion caused by excessive denoising.

(ii) Method advantages: ICEEMDAN decomposition effectively overcame the mode aliasing problem of traditional EMD, laying a solid foundation for an accurate selection of subsequent components. The core innovation lies in introducing GRA as the discrimination criterion for IMF components. By calculating the geometric similarity between each IMF and the noisy original signal, it can adaptively and precisely distinguish between components dominated by noise and those dominated by effective signals, overcoming the rigid judgment defects of traditional methods based on COEFs or fixed thresholds.

(iii) Robustness and universality: Three sets of experiments of different types consistently showed that this method has good adaptability and robustness for seismic signals with different SNRs and characteristics, verifying its great potential as a high-fidelity, adaptive denoising tool in actual seismic data processing.

In summary, the ICEEMDAN–GRA integration technique provides a balanced and effective solution for high-quality pre-processing of node seismometer data, particularly suitable for seismic monitoring and geophysical exploration projects involving small to medium-sized samples. Although this study has achieved some anticipated results, the following aspects warrant further exploration and refinement:

(i) Parameter adaptive optimization: While parameters, such as ICEEMDAN decomposition noise intensity,

ensemble size, and maximum iteration count are effective in the current model, they rely to some extent on empirical settings. Future work should explore integrating intelligent optimization algorithms (e.g., particle swarm optimization, genetic algorithms) with this research model to achieve fully adaptive determination of key parameters, thereby further enhancing the model's automation level and universality.

(ii) Graphics Processing Unit parallel computing: Each noise addition decomposition in ICEEMDAN is inherently independent, presenting a natural parallelism opportunity. Calculations for different IMFs and metrics within GRA can also be parallelized, making the algorithm highly amenable to parallel acceleration on Graphics Processing Units or multi-core Central Processing Units. Near-linear speedup is anticipated.

(iii) High-performance computing and cloud computing: For ultra-large-scale seismic datasets, data can be partitioned and processed in parallel across clusters, thereby reducing the absolute computational time of the model presented in this study.

Acknowledgments

None.

Funding

This research was financially supported by Mahasarakham University; the Scientific Research Fund from the Institute of Seismology, CEA and National Institute of Natural Hazards, Ministry of Emergency Management of China (No. IS202226322, No.IS202436357); the Open Fund of Wuhan Gravitation and Solid Earth Tides, National Observation and Research Station, (No.WHYWZ202406); the Spark Program of Earthquake Technology of CEA (No.XH24025YC, XH25019C); the 2025 Hubei Provincial Key Laboratory Targeted Commissioned Project (No.2025CSA083); research grants from the National Institute of Natural Hazards, Ministry of Emergency Management of China (Grant number: ZDJ2024-31); the 2025 Doctoral Special Support Program Project of Chengdu Jincheng College (NO.2025JCKY(B)0018); and the Mathematics and Finance Research Center Project of Dazhou Social Science Federation Key Research Base (No. SCMF202505).

Conflict of interest

The authors declare they have no competing interests.

Author contributions

Conceptualization: Cong Pang, Tianwen Zhao, Sirui Liu, Xingxing Li, Ya Xiang

Formal analysis: Cong Pang, Guoqing Chen, Tianwen Zhao, Yuxuan Liang, Ya Xiang

Investigation: Tianwen Zhao, Sirui Liu, Yuxuan Liang, Xingxing Li, Piyapatr Busababodhin

Methodology: Cong Pang, Tianwen Zhao, Guoqing Chen, Piyapatr Busababodhin

Writing–original draft: Cong Pang, Tianwen Zhao, Guoqing Chen, Piyapatr Busababodhin

Writing–review & editing: Cong Pang, Tianwen Zhao, Guoqing Chen, Piyapatr Busababodhin

Availability of data

Some data used in this study cannot be shared publicly due to collaborative agreement restrictions but are available from the corresponding author upon reasonable request.

References

1. Baker B, Holt MM, Pankow KL, Koper KD, Farrell J. Monitoring the 2020 Magna, Utah, earthquake sequence with nodal seismometers and machine learning. *Seismol Res Lett*. 2021;92(2A):787-801.

   doi: 10.1785/0220200316

2. Xiong C, Deng Y, Wang L, Ye X, Zhang Y. High-resolution monitoring of Urban activities with nodal seismometers in the Guangdong-Hong Kong-Macao greater bay area, China. *Earth Space Sci*. 2025;12(4):e2024EA004088.

   doi: 10.1029/2024EA004088

3. Nayak A, Verónica RT, Jonathan AF, *et al*. Nodal and broadband seismometer complement to the imperial valley dark fiber DAS array. *Seismol Res Lett*. 2023;94(6):2852-2867.

   doi: 10.1785/0220230081

4. Gaishan Z, Zhanxiang HE. Comprehensive view of the development of nodal seismic technology. *Geophys Prospect Petrol*. 2024;63(4):718-734.

   doi: 10.12431/issn.1000-1441.2024.63.04.002

5. Li YE, Nilot EA, Zhao Y, Fang G. Quantifying Urban activities using nodal seismometers in a heterogeneous Urban space. *Sensors (Basel)*. 2023;23(3):1322.

   doi: 10.3390/s23031322

6. Abbas A, Cox BR, Tran KT, Corey I, Dawadi N. An open-access data set of active-source and passive-wavefield DAS and nodal seismometer measurements at the newberry florida site. *Seismol Res Lett*. 2024;95(2A):1082-1098.

   doi: 10.1785/0220230216

7. Liu S, Yan A, Huang S. Seismic data denoising based on DC-PCNN image fusion in NSCT domain. *IEEE Geosci Remote Sens Lett*. 2024;21:1-5.

   doi: 10.1109/LGRS.2024.3369727

8. Liang C, Lin H, Ma H. Reinforcement learning-based

denoising model for seismic random noise attenuation. *IEEE Trans Geosci Remote Sens*. 2023;61:1-17.

doi: 10.1109/TGRS.2023.3268718

9. Li F, Liu H, Wang W, Ma J. Swin transformer for seismic denoising. *IEEE Geosci Remote Sens Lett*. 2024;21:1-5.

doi: 10.1109/LGRS.2024.3358234

10. Cao M, Hua Y, Zhang J, Zhang H, Ma F, Ji P. Denoising method for ultrasonic echo signal of mining well logging instrument based on NRBO-ICEEMDAN wavelet thresholding. *IEEE Sens J*. 2025;25(15):29700-29710.

doi: 10.1109/JSEN.2025.3578599

11. Chen X, Chen XY, Zhao LY, *et al*. Feature-adaptive self-supervised leaning for microthrust measurement signals' blind denoising. *IEEE Sens J*. 2025;25(1):1015-1028.

doi: 10.1109/JSEN.2024.3493104

12. Qiao J, Ai W, Hu X, Liu M, Hu S. An identification method of melting layer using the covariance wavelet transform based on GPM-DPR observations. *Earth Space Sci*. 2022;9(3):e2021EA002103.

doi: 10.1029/2021EA002103

13. Sun M, Wu J, Lu Y, Yu F, Zhou H. Engineering safety-oriented blasting-induced seismic wave signal processing: An EMD endpoint suppression method based on multi-scale feature. *Sensors (Basel)*. 2025;25(13):4194.

doi: 10.3390/s25134194

14. Zhao Y, Zhong Z, Li Y, *et al*. Ensemble empirical mode decomposition and stacking model for filtering borehole distributed acoustic sensing records. *Geophysics*. 2023;88(1):WA319-WA334.

doi: 10.1190/geo2022-0273.1

15. Ji M, Zhao X, Zhu W, *et al*. Noise attenuation using adaptive wavelet threshold based on CEEMD inf-X domain. *J Seism Explor*. 2023;32(2):131-153.

16. Yin X, Liu Q, Huang X, Pan Y. Development and application of a novel hybrid CEEMDAN-LWT denoising approach in microseismic monitoring. *Pure Appl Geophys*. 2022;179(9):3279-3294.

doi: 10.1007/s00024-022-03115-8

17. Zhang Y, Zhan K, Song P, Liang C, Xu R, Kong C. Improved first arrival picking of microseismic P-waves in coal mines using multi-denoising and adaptive characteristic functions. *Sci Rep*. 2025;15(1):33141.

doi: 10.1038/s41598-025-18503-y

18. Shi Y, Yang C, Wang J, Zhang Z, Meng F, Bai H. A forecasting model of ionospheric foF2 using the LSTM network based on ICEEMDAN decomposition. *IEEE Trans Geosci Remote Sens*. 2023;61:1-16.

doi: 10.1109/TGRS.2023.3336934

19. Li X, Li H, Yang Z, Zhou J, Li H, Bu J. Radiation signal denoising method of loaded coal-rock based on ICEEMDAN-PCK-means-IP. *IEEE Sens J*. 2023;23(19):23103-23118.

doi: 10.1109/JSEN.2023.3306932

20. Nguyen VT, Nguyen MT. Advanced noise reduction for in-cylinder combustion pressure data using ICEEMDAN and optimal wavelet selection. *IEEE Access*. 2025;13:62029-62044.

doi: 10.1109/ACCESS.2025.3558428

21. Esangbedo MO, Xue J, Bai S, Esangbedo CO. Relaxed rank order centroid weighting MCDM method with improved grey relational analysis for subcontractor selection: Photothermal power station construction. *IEEE Trans Eng Manage*. 2024;71:3044-3061.

doi: 10.1109/TEM.2022.3204629

22. He J, Wang H, Wang J, Zuo C, Wang Z, Zhao X. Decision-making method for multiobjective demagnetization strategies of underwater vehicles based on improved gray relation analysis. *IEEE Trans Instrument Measure*. 2024;73:1-13.

doi: 10.1109/TIM.2023.3341120

23. Tan R, Zhang W, Chen S. Decision-making method based on grey relation analysis and trapezoidal fuzzy neutrosophic numbers under double incomplete information and its application in typhoon disaster assessment. *IEEE Access*. 2020;8:3606-3628.

doi: 10.1109/ACCESS.2019.2962330

24. Fu J, Fan R, Cao J, Zhang X, Shi S. Seismic impedance inversion using a joint deep learning model based on convolutional neural network and transformer. *IEEE J Select Topics Appl Earth Observ Remote Sens*. 2023;16:8913-8922.

doi: 10.1109/JSTARS.2023.3318078

25. Yang C, Guan Y, Liu T, Zhang B, Li W. MMI-ML: Maximize mutual information between different views for few-shot remote sensing image classification. *IEEE Geosci Remote Sens Lett*. 2024;21:1-5.

doi: 10.1109/LGRS.2024.3388463

26. Pang C, Ding W, Cheng C, *et al*. Research on seismic discrimination based on particle swarm optimization generalized regression neural network and HHT sample entropy. *Prog Geophys*. 2022;37(4):1457-1463.

doi: 10.6038/pg2022FF0438

27. Mendo L. Estimation of a probability with guaranteed normalized mean absolute error. *IEEE Commun Lett*. 2009;13(11):817-819.

doi: 10.1109/LCOMM.2009.091128

28. Liu N, Wu L, Wang J, Wu H, Gao J, Wang D. Seismic data reconstruction via wavelet-based residual deep learning. *IEEE Trans Geosci Remote Sens*. 2022;60:1-13.

doi: 10.1109/TGRS.2022.3152984

29. Song J, Ntibahanana M, Luemba M, Tondozi K, Imani G. Ensemble deep learning-based porosity inversion from seismic attributes. *IEEE Access*. 2023;11:8761-8772.

    doi: 10.1109/ACCESS.2023.3239688

30. Dou Y, Li K, Lv W, Li T, Xiao Y. ContrasInver: Ultra-sparse label semi-supervised regression for multidimensional seismic inversion. *IEEE Trans Geosci Remote Sens*. 2024;62:1-13.

    doi: 10.1109/TGRS.2024.3410022

31. Pourmirzaee R, Hosseini S. Development of an ANN-based technique for inversion of seismic refraction travel times. *J Environ Eng Geophys*. 2024;29(2):75-90.

    doi: 10.32389/JEEG22-044

32. Yan Y, Chen X, Li J, Guan J, Li Y, Cui S. Multiparameter shallow-seismic waveform inversion based on the Jensen-Shannon divergence. *Geophys J Int*. 2024;238(1):132-155.

    doi: 10.1093/gji/ggae143

33. Kumar DR, Samui P, Burman A, Kumar S. Seismically induced liquefaction potential assessment by different artificial intelligence procedures. *Transport Infrast Geotechnol*. 2024;11(3):1272-1293.

    doi: 10.1007/s40515-023-00327-w